

N 70 43075

CR 110871

MOLECULAR BEAM SURFACE INTERACTION

Final Report

Contract NASw-1588

CASE FILE  
COPY

Prepared for

National Aeronautics and Space Administration

Washington, D. C. 20025

Prepared by

Space Sciences Laboratory

General Electric Company

Box 8555, Philadelphia, Pa. 19101

MOLECULAR BEAM SURFACE INTERACTION

Final Report

Contract NASw-1588

Prepared for

National Aeronautics and Space Administration

Washington, D. C. 20025

Prepared by

Space Sciences Laboratory

General Electric Company

Box 8555, Philadelphia, Pa. 19101

# TABLE OF CONTENTS

| <u>Section</u> |   | <u>Page</u> |
|----------------|---|-------------|
| 1              | INTRODUCTION . . . . .                          | 1           |
| 2              | BACKGROUND . . . . .                            | 2           |
| 3              | APPARATUS . . . . .                             | 4           |
|                | 3.1 New Balance System . . . . .                | 4           |
|                | 3.2 Flux Probe . . . . .                        | 7           |
|                | 3.3 Accommodating Surfaces . . . . .            | 9           |
| 4              | EXPERIMENTAL RESULTS . . . . .                  | 19          |
|                | 4.1 Flux Measurements - First Series . . . . .  | 21          |
|                | 4.2 Flux Measurements - Second Series . . . . . | 22          |
|                | 4.3 Calculations and Discussion . . . . .       | 23          |
| 5              | CONCLUSIONS . . . . .                           | 61          |
| 6              | REFERENCES . . . . .                            | 62          |

## SECTION 1

### INTRODUCTION

The work to be reported here is an extension of the studies initiated under NASw-750 which led to the development of a molecular beam apparatus for the experimental investigation of momentum transfer between neutral particles and solid surfaces. Here, in the second phase, the scope of the investigation was broadened to include (1) higher beam energies, (2) varying angles of incidence, (3) wider selection of surface conditions, and (4) measurements of the spatial distribution of the reflected particles.

In this program, surfaces of technical interest were investigated, i.e., rough, contaminated surfaces in addition to the somewhat idealized smooth, clean cases. The objective is to obtain data which has application to practical situations, e.g., the calculation of drag, as well as the idealized cases which are primarily of theoretical interest.

## SECTION 2

### BACKGROUND

The energy and momentum exchange which occurs when an individual molecule interacts with a solid surface is a matter of considerable scientific and practical interest. Some thermal accommodation data are available from studies employing solids whose surface states were well enough known to attempt theoretical correlations with gas molecule-solid surface forces and solid-state properties of the lattice.<sup>(1)</sup> On the other hand, measurement of momentum exchange is capable of giving more detailed information regarding the molecule-surface interaction process than the measurements of thermal accommodation, which comprise the bulk of measurements made to date, particularly if the distribution of scattered particles is also known.

Data concerning momentum exchange between individual molecules and solid surfaces are basic to the understanding of atmospheric drag on artificial satellites of the earth and other planets.<sup>(2)</sup> Although air drag on earth satellites has customarily been neglected above a few hundred miles altitude for most calculations of satellite trajectories, these effects can become important for problems of relative motion between neighboring satellites, for forces and torques acting on large space structures, and for satellites designed for extremely long lifetimes. Drag forces which may be negligible for the problem of computing the position of the satellite may become important when discussing the relative motion of two neighboring satellites with large differences in cross section or mass, where slight differences in drag may have a major effect on the relative motion. Such effects may already have been encountered in the case of multiple satellites launched from the same booster.<sup>(3)</sup> Although for such practical problems it would be most useful to know the momentum accommodation between atmospheric species and technical surfaces, so little data exist that it will be necessary to first make measurements under highly controlled laboratory conditions where the molecular species and surfaces are precisely known. Thus, some of the important systematics can be established before more complicated problems such as momentum exchange involving excitation of diatomic molecules, contaminated surfaces, etc. can be successfully attacked.

Another area in which increased understanding of the interaction between high velocity molecules and surfaces is important is in satellite instrumentation for measurements of pressure and composition. Here it would often be useful to know, for example, the loss in molecular speed after a single collision within the instrument or the speed with which molecules leave the vicinity of a spacecraft after collision with the spacecraft surface. Knowledge of the energy accommodation at high molecular velocities is also necessary to predict gaseous heat transfer to instruments or space vehicles operating at relatively low altitudes. Work to date has led to the development of a molecular beam apparatus and the associated balance apparatus for the experimental investigation of momentum transfer between neutral particles and solid surfaces. The beam is produced in a cryogenically pumped vacuum system using a 2 kw helium refrigerator operating at 16°K. Under steady-state conditions, the pumping speed at  $10^{-7}$  torr is in excess of  $10^8$  litres/sec. This vacuum system contains equipment for producing nozzle beams from a gas source which can be operated between 78 and 2600°K and a torsion balance with a sensitivity of  $10^{-5}$  dynes for measuring momentum exchange.

The calculation of momentum accommodation coefficients is calculated from two basic force measurements. One is obtained from the interaction of a directed beam with the surface of interest and the second from a "virtual surface" designed to afford complete energy and momentum accommodation for the same incident beam. This virtual surface is defined by the area bounded by the periphery of an opening to a cavity which otherwise is closed. Nearly all incident beam particles accommodate completely to the temperature of the enclosure since they must make many collisions with the walls before effusing back through the opening. It is assumed that the effluent particles leave the cavity with a cosine distribution. All force measurements are made at null displacement. The restoring torque is supplied by an external magnetic field acting on a small bar magnet. The force required to maintain a null position is measured in terms of the current passing through the Helmholtz field coils. The experimental surface is prepared, in situ, by vapor deposition from an oven enclosed in the vacuum system. As previously reported under NASw-750, exploratory measurements have been made of the normal momentum transfer coefficients for Ar on vapor-deposited gold and Ar on untreated mica as a function of source temperature.

## SECTION 3

### APPARATUS

During the period of this contract, basic changes were made in the design of the momentum balance and additional apparatus was installed to measure flux distribution of the reflected particles.

#### 3.1 NEW BALANCE SYSTEM

Previously, all force measurements were made with a double balance arrangement. One balance was used for beam-target interaction measurements and the other carried a cavity for making reference measurements at unit accommodation. The main limitation of this system was that observations were restricted to normal incidence. To investigate momentum transfer at various angles of incidence, a method for rotating the target was devised. This arrangement (see Figure 1) also made it possible to combine the target and cavity into a single structure, thus eliminating the need for a second balance. This simplification also enhances the accuracy of the measurements since it is no longer necessary to know the relative values of the individual balance constants.

The target-cavity structure is a rectangular parallelepiped (2.2 cm long x 1.0 cm wide x 1.0 cm deep) with a circular opening, 0.64 cm diameter, in the center of one face. The target substrate is a mica, lamina 0.01 cm thick mounted on brass plate (0.02 cm thick) by metal clips. The other five walls of the cavity structure are made from 75  $\mu$  stainless steel foil, spot welded at the seams. The balance is suspended by an 18  $\mu$  tungsten filament 10 cm in length. When the beam enters the cavity through this aperture, the incident molecules will make many collisions with the interior surfaces before escaping. If, (1) the total surface area to aperture ratio is large, (2) the diameter of the aperture is large compared with the material thickness at the periphery, and (3) the mean free path of the molecules within the cavity is much larger than the physical dimensions, then the molecules will leave the cavity effusively and with a cosine distribution. In effect, the aperture will behave as a virtual surface with unit accommodation.

The torsion balance itself is shown in Figures 2 and 3 for both the box normal and target normal positions. A copper-constantan thermocouple is spot welded to the interior of the box and the two leads are brought out to sleeves A and B which are otherwise electrically isolated from a common shaft by Lexan bushings. This shaft passes through a fixed tubular section, C, and carries an arm for the angular positioning of the target.

The angle of incidence (i. e. , angle of attack) is changed by rotating the target assembly. To do this it is necessary to cage the balance. A caging fixture, Figure 4, which is raised by an eccentric cam first engages the two locating cylinders, thus preventing all motion transverse to the balance axis. As the fixture continues to move upwards, the cross arm is engaged by two V-shaped hooks which act as a cradle. The final portion of the caging cycle lifts the whole balance about one millimeter, thus producing slack in the suspension to protect it from any mechanical disturbance. The eccentric cam is driven by 6 rpm induction timing motor with a built-in magnetic brake. Two cams mounted on the driving shaft operate switches which automatically stop the motor in either the caged or uncaged position once the circuit has been closed by an external override control. Since the ambient temperature in the cryo-chamber is of the order of  $15^{\circ}\text{K}$ , the motor, clutch, and gear train must be heated to function. Nichrome resistance wire embedded in asbestos is used to cover the motor casing to maintain a temperature in the range of  $260$  to  $270^{\circ}\text{K}$ . This requires a power input of approximately 7 watts. The motor that drives the target positioning arm is also provided with a heating jacket. The use of Teflon bearings in the right angle gear train ensures low frictional resistance, even at the lowest temperatures and pressures. The target can be set at any desired angle of incidence; however, for convenience three cam switches are provided to establish the most commonly used angles, i. e. , box normal and plate normal with respect to the beam, and plate parallel to the exit aperture of the gold vapor source. The target temperature is determined while in the caged position by making contact with the thermocouple leads through the two supporting hooks.

The complete assembly, including the motors previously described and all other auxiliary components, is shown in Figures 5 through 7 mounted on a bench test stand. The major items are labeled and for the most part are self explanatory. All force measurements are



made in terms of the field coil current required to bring the galvanometer light spot to a reference position on the ground glass scale, at which point the cross arm of the balance is normal to the beam axis. Although the original balance was provided with a damping mechanism, this was subsequently eliminated when tests showed that observations could be taken more rapidly and accurately without it.

To the extent that the primary objective of the experimental program is to obtain ratios of the force exerted on the target plate (for varying angles of incidence) to that exerted on the cavity, no calibration is necessary. All mechanical and geometrical constants cancel out in the ratios. However, if one wishes to know the magnitude of the incident flux, then a calibration must be made. For this reason, and in the interests of a complete experimental evaluation of the apparatus, the various constants were determined as follows:

The torsional spring constant,  $k$ , of the suspension is determined prior to installation. Each end of the filament is spot welded to a metal tab for mounting purposes. One tab is fastened to a support and the period of oscillation,  $T_o$ , due to the other is noted. Then a slender rod of mass,  $M$ , and length,  $L$ , is fastened horizontally at the midpoint to the lower tab and the new period,  $T_1$ , is determined. From these data  $k$  can be calculated, i. e. ,

$$k = \frac{2}{3} \frac{ML^2}{(T_1^2 - T_o^2)}$$

Next the balance is assembled and the incremental displacement,  $\Delta D$ , of the light spot is measured as a function of field coil current,  $\Delta I$ . If the angular displacement is small, the ratio  $\Delta D/\Delta I$  should be a constant, say  $C_1$ . This is found to be the case. From the geometry of the apparatus the angular displacement corresponding to  $\Delta D$  can be determined, thus we have another constant,  $C_2$ . If the moment arm, measured from the balance axis to beam axis, is  $\ell$ , then the relationship between the force on the target and restoring current  $I$  is given by

$$F = \frac{C_1 C_2 k}{\ell} I$$

which in dimensional form is:

$$F(\text{dynes}) = \left( \frac{\text{cm}}{\text{ma}} \right) \cdot \left( \frac{\text{rad}}{\text{cm}} \right) \cdot \left( \frac{\text{dyne-cm}}{\text{rad}} \right) \cdot \left( \frac{1}{\text{cm}} \right) I (\text{ma})$$

Typical values for these constants are  $-C_1 = 0.13 \text{ cm/ma}$ ,  $C_2 = 0.0198 \text{ rad/cm}$ ,  $k = 0.13 \text{ dyne cm/rad}$ , and  $\ell = 2.22 \text{ cm}$ . For a representative situation we have

$$F = 1.65 \times 10^{-4} I$$

where the sensitivity is of the order of  $10^{-5}$  dynes.

The target is maintained at a constant temperature by a 650-watt quartz projection lamp. A massive copper housing is provided to shield the cryogenic surfaces from the excess radiation and to act as a heat sink.

### 3.2 FLUX PROBE

From measurements of the force exerted on the target surfaces at various angles of incidence, it became apparent that the null balance conditions were not compatible with a Knudsen flux distribution for the reflected particles. This was found to be the case for nearly all grazing angles and in many instances for normal incidence as well. Clearly, the next step, from both experimental and theoretical points of view, was to ascertain the shape of the distribution. This information is needed for comparison with the findings of other investigators who have been involved primarily with the measurement of distributions per se. It would be highly desirable to obtain in a single experiment both the shape of the distribution and the integrated momentum transfer rate. To this end, a probe has been constructed for measuring flux both in and out of the plane which includes the surface normal and beam axis.

The pressure probe arrangement shown schematically in Figure 8 allows measurements to be taken about two axes. The axis A-A' (which is coincident with the balance cross arm) is mutually perpendicular to the beam axis and the normal to the target surface. Rotation about B-B' provides for the out-of-plane measurements. The geometry is such that the axis of the probe always passes through a fixed point in the target surface regardless of the rotation about A-A' or B-B'. These angular displacements are designated by  $\Theta$  and  $\psi$  respectively. Angle  $\Theta$  is taken as zero when the probe is in the beam axis looking in the direction of the beam. All values of  $\Theta$  between 14 and 180 degrees are accessible, the smaller angle being determined by the dimensions of the probe itself. Out-of-plane measurements,  $\psi$ , can be made within the range of 0 to 30 degrees. Both the  $\Theta$  and  $\psi$  positions can be changed continuously during the course of the experiment.

For source pressures at which we desire to operate, i. e. , 30 to 50 torr, the beam intensity at the target,  $I_t$ , should be approximately  $2 \times 10^{14}$  mol/sec according to previous calculations. Assuming diffuse reflection, the number of particles entering the probe orifice area,  $A_p$ , will be

$$I_p = \frac{4 f A_p I_t}{\pi d^2} \quad (1)$$

where  $f$  is a geometrical parameter related to the view factor. Thus for  $d$  equal to 3.2 cm we have

$$I_p = 2.5 \times 10^{13} f A_p \quad (2)$$

The pressure within the guage can be estimated by considering the probe as an extension of a Knudsen oven. Applying the conservation of mass flow in both directions through  $A_p$ ,

$$I_p = \frac{K 3.52 \times 10^{22} p}{(MT_p)^{1/2}} \quad (3)$$

where  $p$  and  $T_p$  are the gauge pressure (torr) and temperature ( $^{\circ}\text{K}$ ) respectively.  $M$  is the molecular weight and  $K$  is the Clausing factor. Combining Equations 2 and 3 we obtain

$$P = 0.633 \times 10^{-7} \frac{f}{K}$$

for  $M = 40$  and  $T_p = 200^{\circ}\text{K}$ .

Reasonable estimates for  $f$  and  $K$  are 0.5 and 0.2 respectively, thus the signal level should be of the order of  $10^{-7}$  torr. Since a background pressure of  $10^{-10}$  torr can be maintained in the cryogenic vacuum changer under steady-state beam conditions, this signal should be adequate. Attempts to raise the temperature of the enclosure are likely to be self-defeating because of outgassing. Since the latter might well increase at a more rapid rate than the signal level, a fairly low value of  $T_p$  is chosen.

### 3.3 ACCOMMODATING SURFACES

If it were possible to find a fully accommodating surface to replace the cavity or "momentum trap," a considerable experimental simplification could be effected. Not only is the cavity structure awkward because of the volume it occupies but it also makes a major contribution to the moment of inertia of the balance system. The purpose of this experiment was to ascertain the accommodating coefficients,  $\alpha$ , for several rough, dirty surfaces with the object of substituting one of them for the cavity presently used.

A cavity with a hexagonal cross-section, Figure 9, was substituted for the rectangular box used in previous experiments. The basic structure was made of 1/2-mil stainless steel, spot welded at the seams. Test surfaces were mounted on four of the faces while the two remaining ones, diametrically opposed, were used for the beam aperture and mica window, the latter being installed for purposes of alignment. Three of the test surfaces were metal, i. e., aluminum, brass, and beryllium copper, while the fourth was of colloidal silver painted on a mica lamina. Only conducting surfaces were used in order to avoid the accumulation of static charge, a problem encountered in the past with dielectric materials. The metal target surfaces were roughened by a liquid honing process which produces a matte finish similar to sand blasting. The scale of roughness, measured optically, was of the order of 5 microns. Except for the hexagonal cavity, no other changes were made in the balance system.

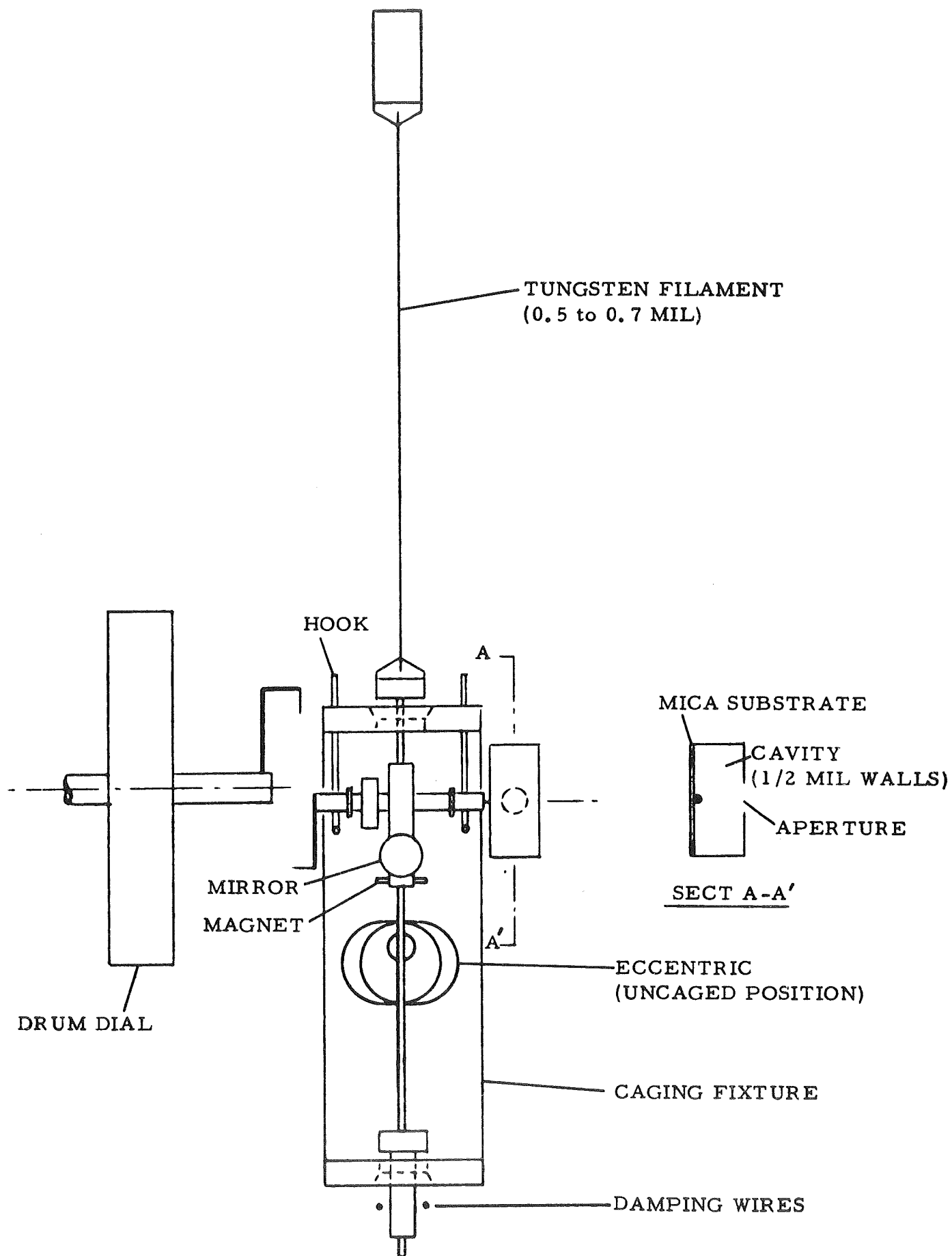


Figure 1

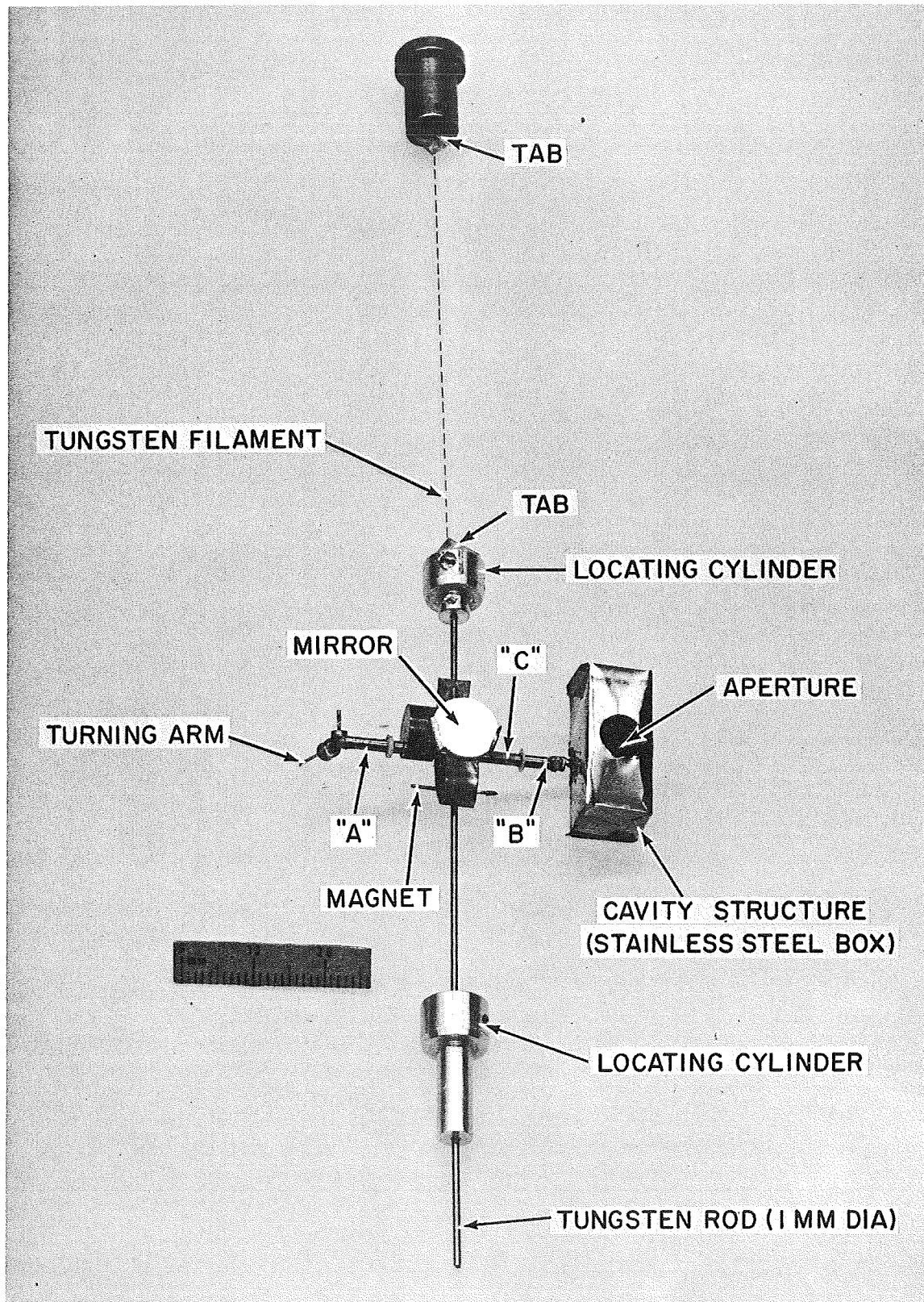


Figure 2

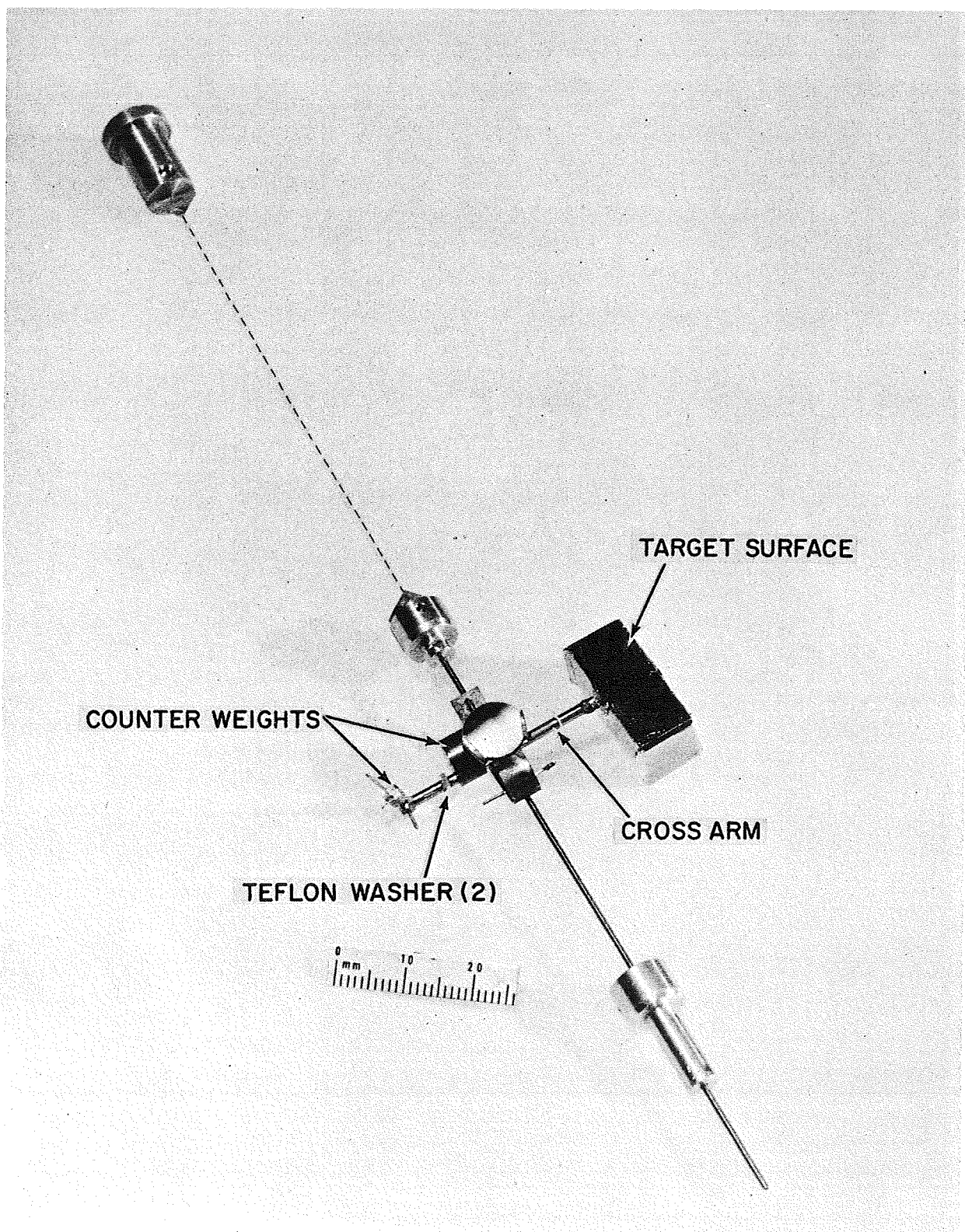


Figure 3



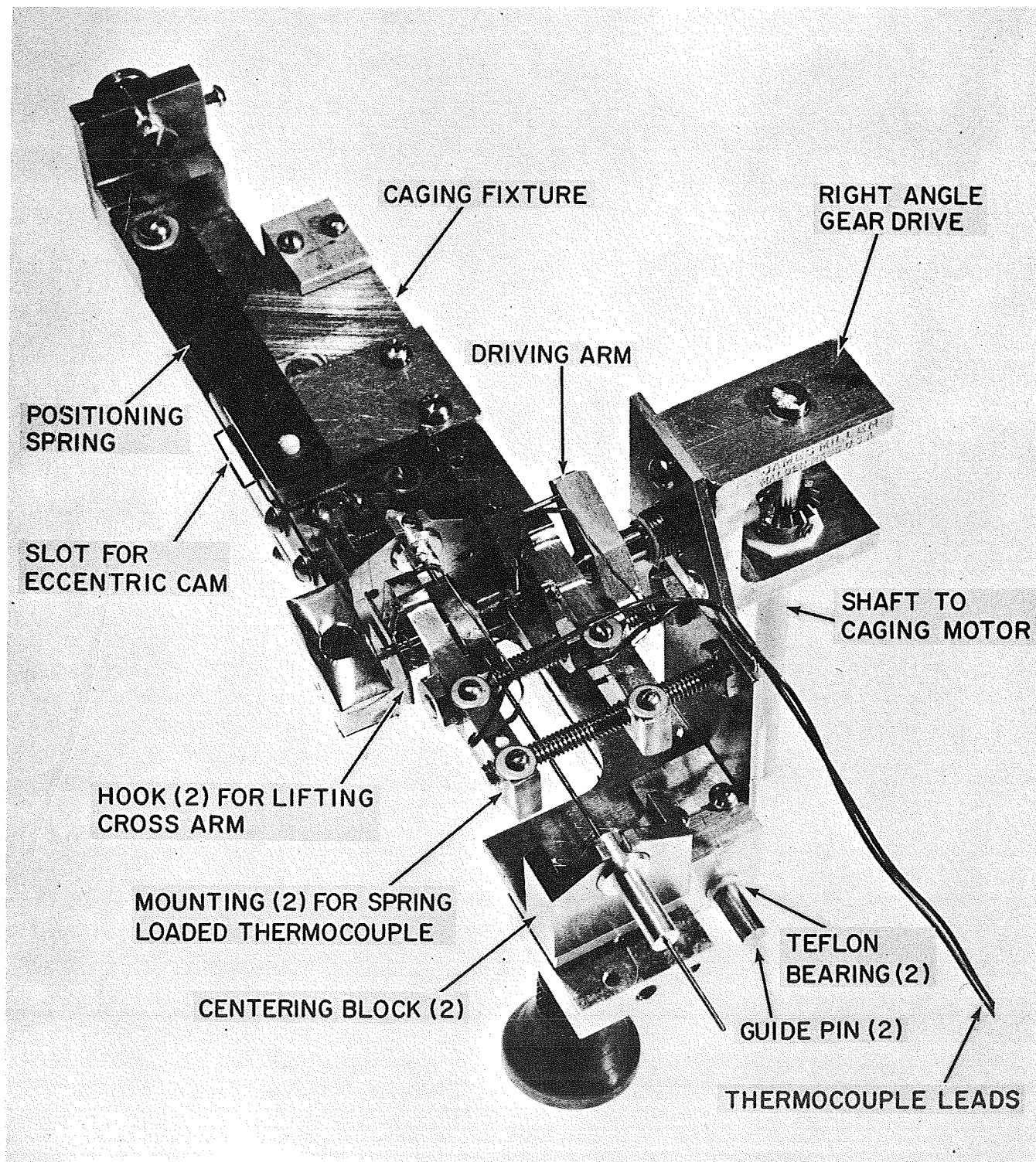


Figure 4



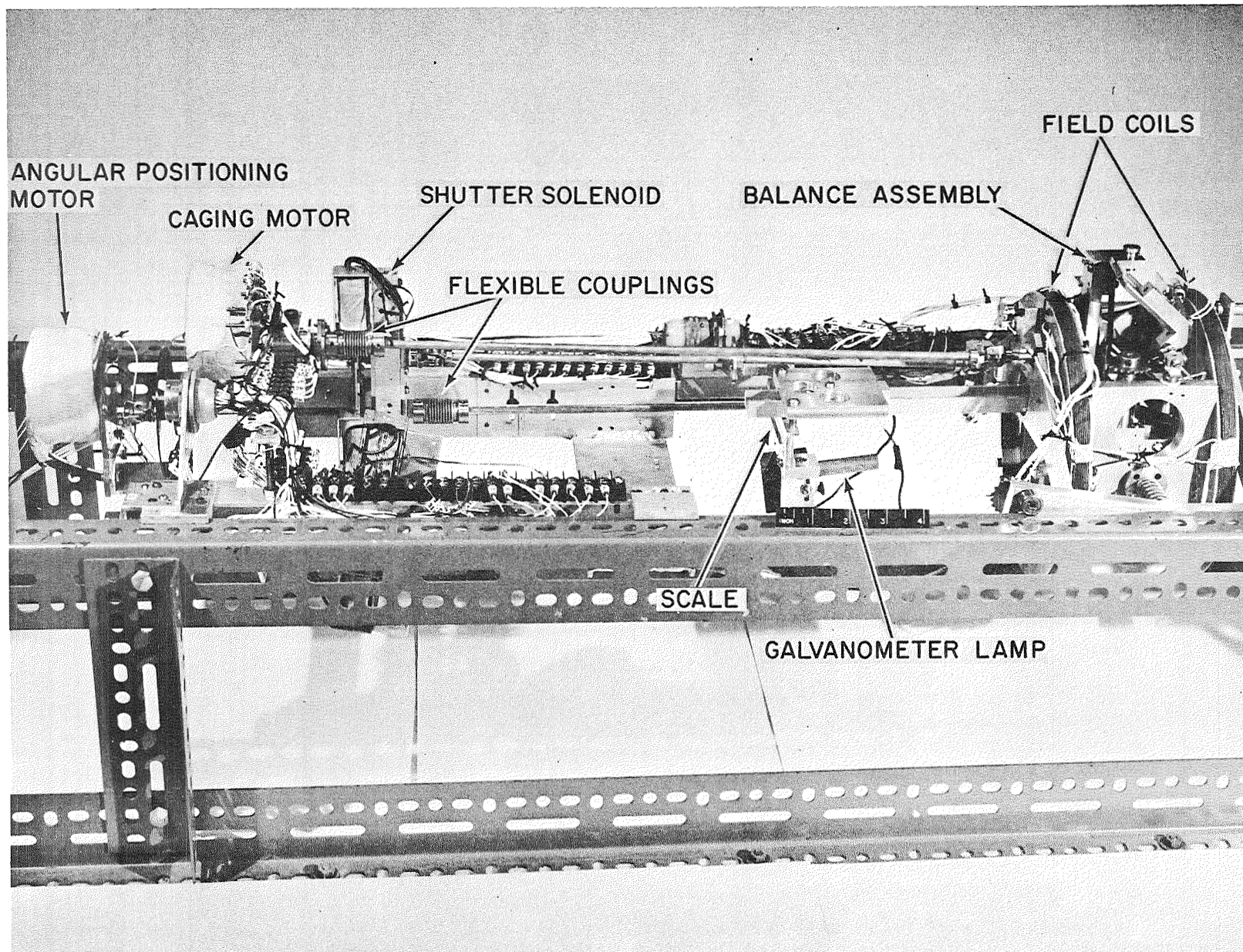


Figure 5

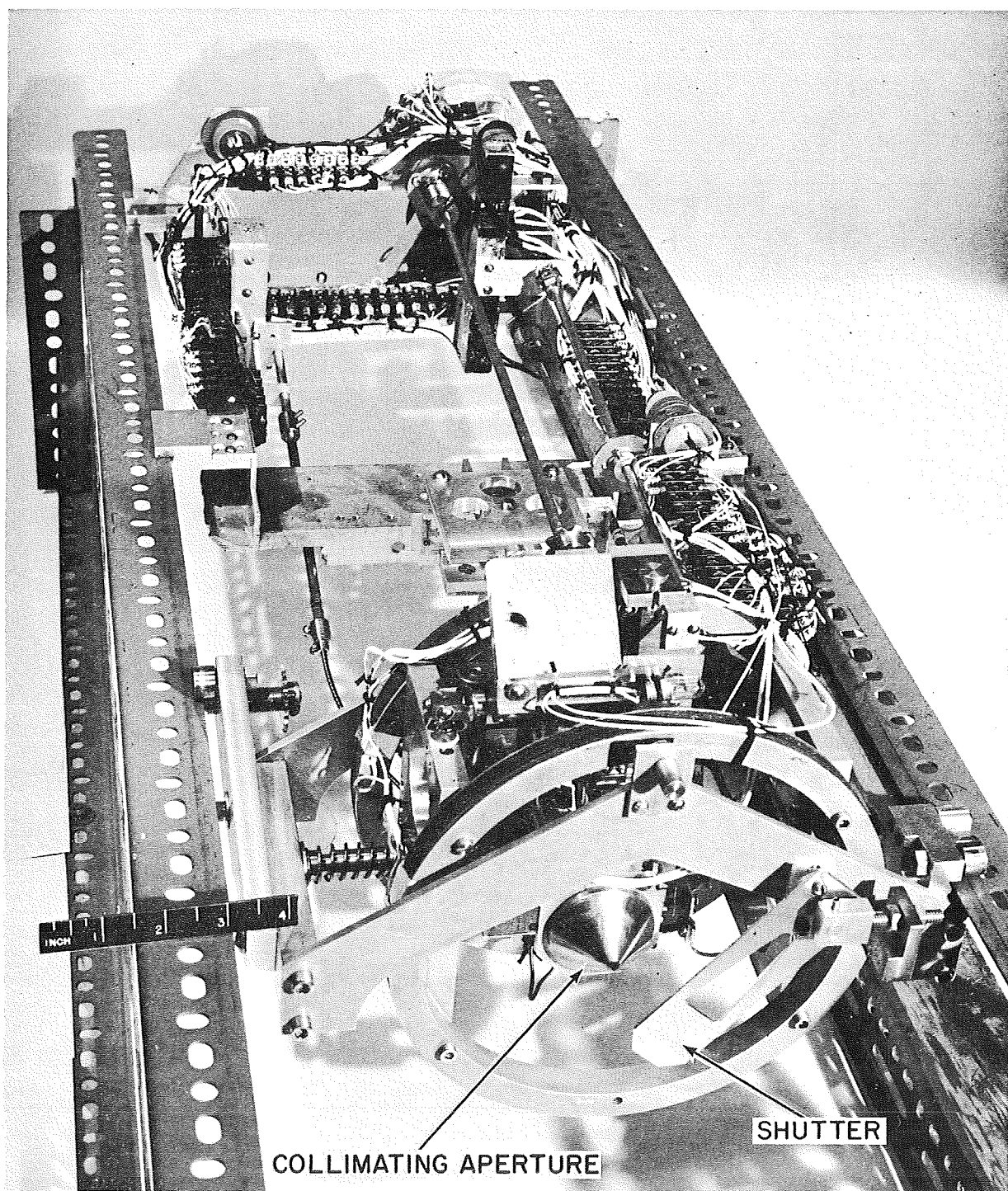


Figure 6

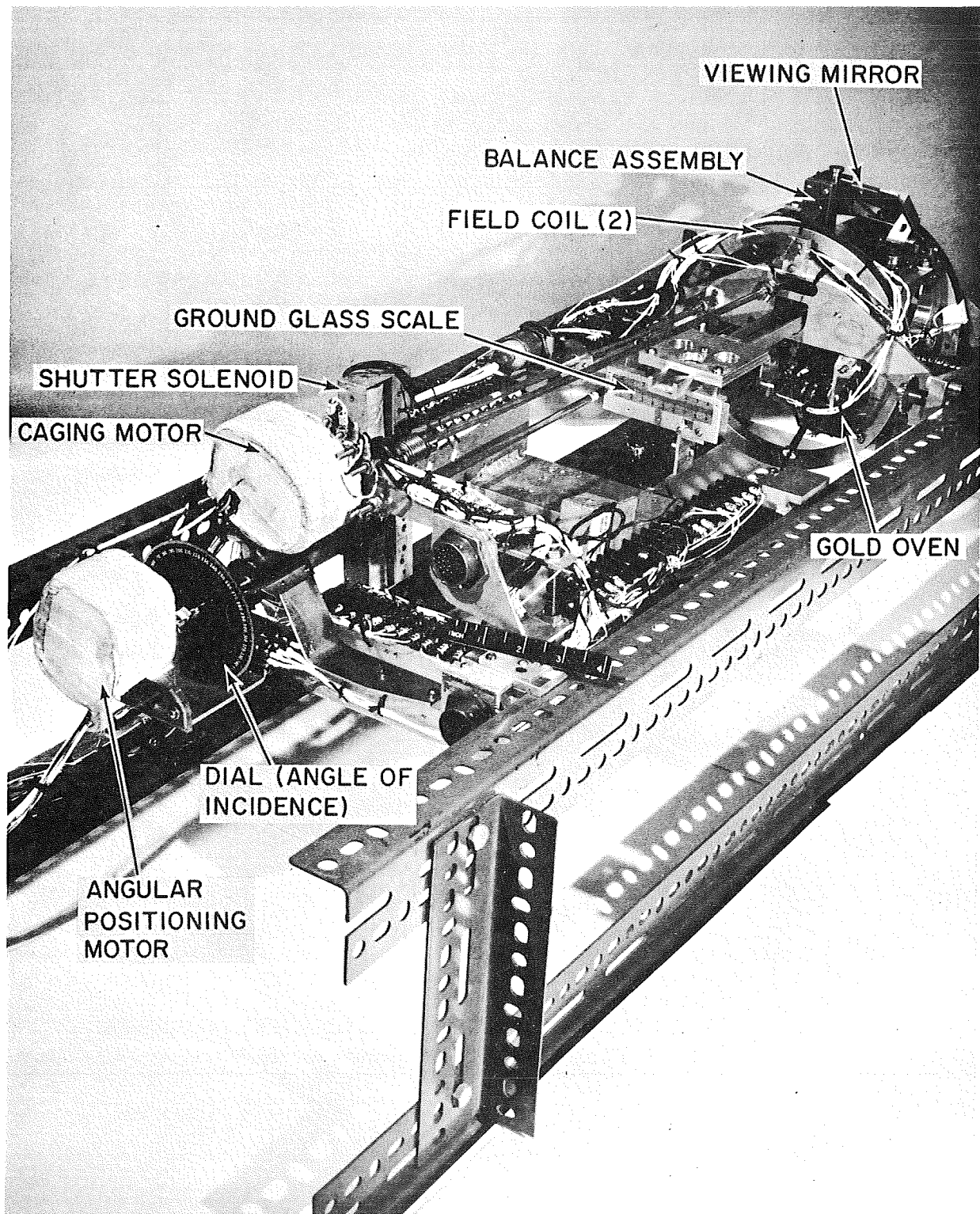


Figure 7

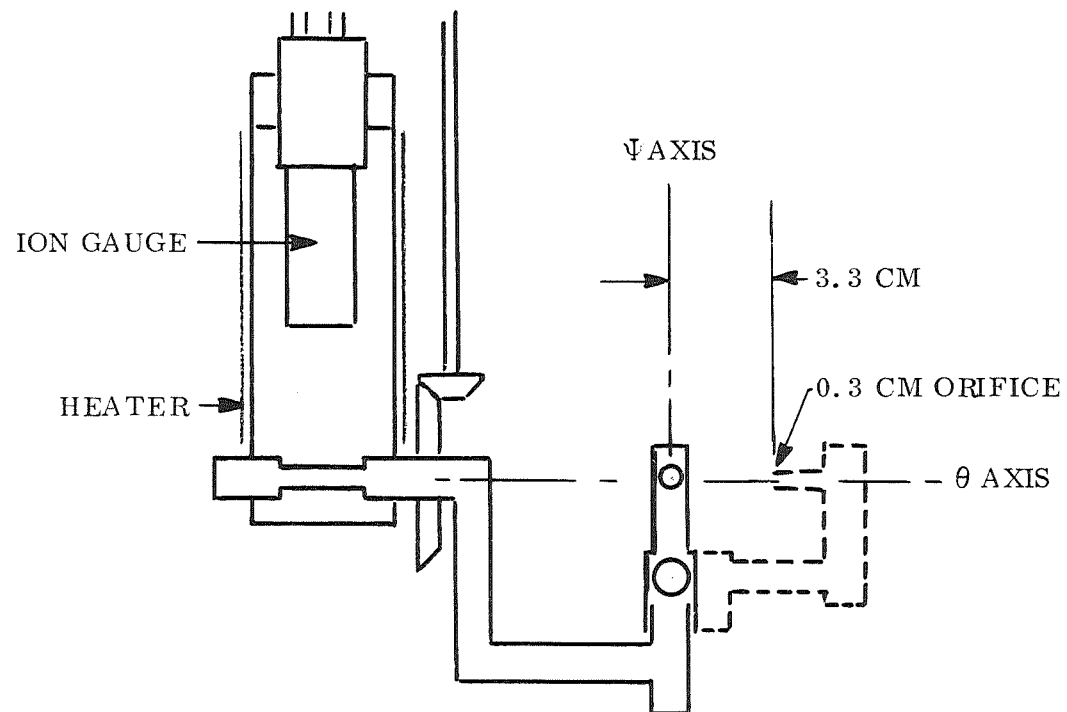


Figure 8 . Pressure Probe Arrangement



COLLIMATING APERTURE

AXIS OF BALANCE ARM

MICA WINDOW

BEAM

(2)

(3)

(6)

(5)

TEST SURFACES

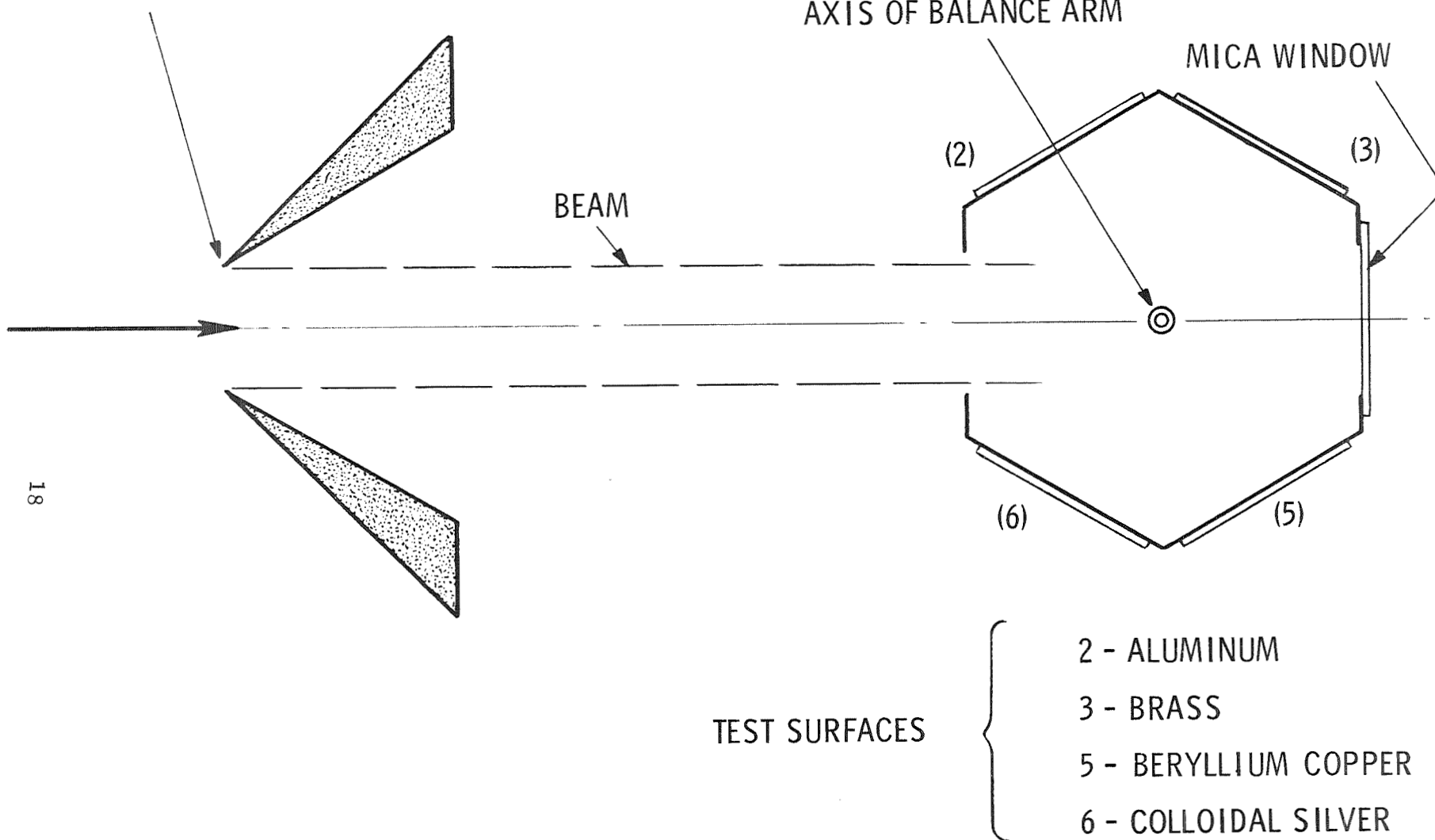
2 - ALUMINUM

3 - BRASS

5 - BERYLLIUM COPPER

6 - COLLOIDAL SILVER

Figure 9



## SECTION 4

### EXPERIMENTAL RESULTS

Momentum exchange data for argon and krypton, impinging at various angles of incidence on clean gold surfaces, are presented in Figure 10. (A single point for nitrogen is also given for normal incidence.) No attempt was made to form extended crystalline formations. It appears that, on a macroscopic scale at least, the target material is in an amorphous state. In all cases, the component of force parallel to the beam is measured, i.e., the drag,  $F_{\odot}$  for any given angle of incidence,  $\odot$ . It is convenient to express these forces in terms of a dimensionless parameter  $R_{\odot}$  defined by the ratio  $F_{\odot}/F_c$  where  $F_c$  is the force exerted on the cavity. Furthermore, in dealing with  $R_{\odot}$ , all mechanical and geometrical constants of the apparatus cancel out.

In general, data were taken with the following ranges of operating conditions: (1) source temperature 280 to 2000<sup>o</sup>K, (2) surface temperature 210 to 250<sup>o</sup>K and (3) angles of incidence, mostly 0, 45, and 72 degrees with some data at 30 and 60 degrees. Data were limited to source temperatures below 1540<sup>o</sup>K due to distortion of the tantalum resistance heater arising from unforeseen stresses. Additional data are given in Table I.

Momentum exchange data for argon and krypton incident on clean silver surfaces are given in Figure 11 for several angles of incidence. Some discrete points for nitrogen-silver and argon-mica interactions are also shown.

Unlike the optically smooth surfaces previously generated with gold and aluminum, the silver deposit appeared to be quite granular. The grains were irregular in shape with the longest dimension being for the most part between 10 and 50 microns. No attempt was made to determine if the grains had a crystalline micro-structure. An optical image could be formed by reflection from the silver deposit; however, the quality was poor.

The force ratio,  $R_{\varnothing}$ , shows remarkably little variation with the kind of incident particle, either as a function of angle,  $\theta$ , or source temperature. Individual data points were

reproducible to within 1 percent, whereas the scatter reflects changes in the surface with time and differences between one deposit and another. Since no systematic change could be discerned from one condition to another, all the data are presented on a single plot and the points averaged out by a single curve.

The fact that  $R_\phi$  is quite insensitive to the nature of the incident particle suggests that momentum exchange is determined more by the topology of the surface rather than by the intrinsic particle-surface properties. Gold surfaces, on the other hand, exhibit quite the opposite behavior.

The variation of  $R_\phi$  with  $\phi$  is given for argon (see Figure 12) at two different source temperatures. Here the broken lines represent the case of complete accommodation with diffuse reflection at the corresponding temperatures. It can be seen that at the higher temperature  $R_\phi$  departs significantly from the diffuse case both at normal and grazing angles.

The data for argon (Figure 13) incorporate the results of three runs conducted at different times and with different surfaces. The data for the other angles of incidence were obtained from a single run. In this figure, the broken lines are the calculated values of  $R_0$  and  $R_{75}$  for the case of a cosine scattering distribution with complete thermal accommodation. The krypton data (Figure 14) follow a trend observed in previous experiments, namely, the  $R_0$  values pass through a broad maximum around 1500°K. Here again the broken lines correspond to complete accommodation with diffuse reflection. The general behavior of  $R_\phi$  with the incident angle (Figure 15) shows that the argon interaction is decidedly more specular than for krypton. This is in accord with earlier experimental findings.

Although the entire balance assembly, including the cross-arm and cavity, was grounded during the entire experiment, a certain amount of drift characteristic of that caused by electrostatic charging was observed. This had no serious effect on the force measurements but did require frequent calibration and null point determinations. The puzzling aspect was how charge was being accumulated if indeed the apparatus was grounded. Subsequent examination of the vapor-deposited surface revealed that there was no electrical contact

between the metallic film and the rest of the balance structure. It turned out that the tabs which hold the mica substrate in place cast a shadow during the vapor deposition process, thus preventing the gold from making contact with ground.

In all previous runs, the first layer of target material was deposited on the mica substrate after the balance was placed in the cryogenic vacuum system. Thus, the initial force measurements were always made with a clean surface. The procedure followed for this run was to expose a freshly deposited gold surface to the laboratory atmosphere for 24 hours prior to installing the apparatus in the main vacuum chamber. By this means a dirty surface was generated which is hoped would approximate conditions encountered in the preparation of actual spacecraft components.

Since the balance could not be removed from the cryogenic chamber for the deposition of aluminum, measurements on this material were first made with the clean surface. Contamination was effected by bringing oxygen into the system through the beam source. It is estimated that a 3-minute exposure to the oxygen beam was sufficient to form an oxide layer.

Force ratio values as calculated from the target and cavity force measurements are presented in Table I for two angles of incidence. These are given in chronological order and the sequence of surface conditions is indicated accordingly.

Results obtained for the rough, contaminated surfaces are summarized in Table II. As previously mentioned in the section dealing with apparatus, it was hoped that one or more of these surfaces would be sufficiently accommodating to provide a substitute for the cavity structure.

#### 4.1 FLUX MEASUREMENTS, FIRST SERIES

These results, along with all subsequent data reported here, are given as recorded. Corrections for view factor, etc., will be treated in subsequent reports as the analyses are completed. Target and pressure probe temperatures were maintained at 320 and 240<sup>0</sup>K



respectively throughout the entire run. The large error bars in Figure 16a reflect efforts to stabilize the system during the preliminary checkout period. By the time out-of-plane measurements were made (Figure 16b), drift and random fluctuations were considerably reduced. In this case, the out-of-plane measurements were made at an inclination,  $\Theta_c$ , of 45 degrees. By definition, the "in plane" (i.e., principal plane) included both the beam axis and the normal to the target surface formed at the point of beam-target intersection. This point of interception is by design coincident with the axis of target rotation. Out-of-plane measurements are given in terms of  $\psi$ , the angle formed by the principal plane and a line passing through the probe and the point of beam-target intersection. As indicated, this transverse plane, in general, makes an angle  $\Theta_c$  with the target normal. The distribution for normal incidence is shown in Figure 16.

All the data in Figure 17 were obtained within a 20-minute interval following the vapor deposition of a 300 Å layer of gold. The two distributions show the effect of a change in source temperature. Out-of-plane data taken for the low and high temperature cases ( $\Theta_c$  equal to 30 and 50 degrees respectively) are given in Figure 17. As in the subsequent measurements, the background pressure did not exceed  $10^{-10}$  torr at any time. Force ratio measurements were also made to determine drag for the high temperature case. Values for two angles of incidence, 0 and 70 degrees, are normalized to that obtained for the fully accommodating cavity,  $F_c$ . The ratios  $F_o/F_c$  and  $F_{70}/F_c$  turned out to be 1.085 and 0.76 respectively. These values are typical of those obtained in the past. They are included here to establish the consistence of the force and scattering data. Distributions taken hours after deposition of the gold are given in Figure 18. Data taken at a 40-degree angle of incidence are shown in Figure 19. At this time, the gold surface was 24 hours old.

#### 4.2 FLUX MEASUREMENTS - SECOND SERIES

As a matter of standard procedure, preliminary measurements were made with the mica-substrate prior to vapor deposition of the target material. This is done for purpose of calibration and to establish experimental consistency with previous results as exhibited by Figure 20. The argon-mica data in Figures 21 and 22 were taken in connection with the force measurements in Figure 23. The latter is included as a typical example of the plots

from which the force ratios are obtained. The values of  $R_o$  and  $R_{70}$  for this case are 1.02 and 0.738 respectively. Nitrogen data (Figures 24 and 25) are also in line with previous observations. The data presented in Figure 26 (a) for a source pressure of 40 torr were completed 15 minutes after deposition of the gold surface. About the same time interval was required to obtain the data for normal incidence, also at 40 torr source pressure. The data at 60 torr were taken immediately afterwards. The actual elapsed time,  $t$ , is noted on this and all subsequent figures. Figures 27 through 33 present the data taken for the balance of this series. In all cases the magnitude of the experimental error is given by the size of the data point circles.

#### 4.3 CALCULATIONS AND DISCUSSION

To calculate  $\alpha$  from the force data, not only must the incident momentum flux be known but also the spatial distribution of the reflected molecules.

For monatomic molecules there is a considerable body of experimental evidence that those in the incident beam are nearly monoenergetic, i.e., the spread in velocity is very small compared to the directed velocity. The total incoming flux of momentum is therefore

$$\dot{M}_i = A_B m \Phi_i \bar{v}_i$$

where  $A_B$  is the cross-sectional area of the beam,  $m$  is the mass of each molecule,  $\Phi_i$  is the number flux and  $\bar{v}_i$  is the average incident velocity.

When the aperture of the cavity is normal to the beam, all the molecules enter and are thermally accommodated to the wall temperature prior to effusing out. This effusive flow carries momentum away at the rate

$$\dot{M}_c = A_c m \Phi_c \bar{v}_x$$

where  $A_c$  is the area of the cavity aperture,  $\Phi_c$  is the effusive flux and  $\bar{v}_x$  is the x-component of the particle velocity. If the molecules leave the box with a cosine distribution in  $\Phi$ ,

then the average velocity in the beam direction  $\bar{v}_x$  is just equal to  $2/3 \bar{v}_c$ , where  $\bar{v}_c$  is the average of the Maxwellian velocity distributions characteristic of the cavity temperature,  $T_c$ . The coefficient results from the integration of a cosine squared function. The net force,  $\vec{F}_B$  acting on the box is

$$\vec{F}_B = \dot{\vec{M}}_i - \dot{\vec{M}}_c$$

or

$$F_B = A_B m \Phi_i \bar{v}_i + \frac{2}{3} A_c m \Phi_c \bar{v}_c$$

now the conservation of mass requires

$$m A_B \Phi_i = m A_c \Phi_c$$

Therefore

$$\begin{aligned} F_B &= A_B m \Phi_i v_i + \frac{2}{3} A_c M \frac{A_B}{A_c} \Phi_i \bar{v}_c \\ &= A_B m \Phi_i \left( v_i + \frac{2}{3} \bar{v}_c \right) \end{aligned}$$

Similarly the force on the target surface for the beam at manual incidence is

$$F_o = A_c m \Phi_i (\bar{v}_i + \lambda \bar{v}_r)$$

where  $\lambda$  is a coefficient dependent on the distribution of scattered particles. It is generally accepted that the magnitude lies between  $2/3$  and  $1$  depending on whether the distribution is cosine or completely specular

According to the definition of  $\alpha$  we have

$$\alpha = \frac{T_i - T_r}{T_i - T_c} = \frac{\frac{-2}{v_i} - \frac{-2}{v_r}}{\frac{-2}{v_i} - \frac{-2}{v_c}}$$

or

$$v_r = \left[ \frac{-2}{v_1} - \left( \frac{-2}{v_i} - \frac{-2}{v_c} \right) \right]^{1/2}$$

$$F_o = A_B m \Phi_i \left( \bar{v}_c + \lambda \left[ \frac{-2}{v_i} - \alpha \frac{-2}{v_i} - \frac{-2}{v_c} \right] \right)^{1/2}$$

and taking the ratio

$$\frac{F_o}{F_B} = \frac{\bar{v}_i + \lambda \frac{-2}{v_i} - \alpha \frac{-2}{v_i} - \frac{-2}{v_c}}{\bar{v}_i + 2/3 \bar{v}_c}^{1/2} = R_o$$

or

$$R_o = \frac{1 + \lambda \left[ 1 - \alpha (1-r)^2 \right]^{1/2}}{1 + \frac{2}{3} r}$$

where

$$r = \bar{v}_c / \bar{v}_i = \frac{3/4 \left( \frac{2 k T_c}{m} \right)^{1/2}}{\left( \frac{5 k T_i}{m} \right)^{1/2}} = 0.77 \left( \frac{T_c}{T_i} \right)^{1/2}$$

and solving for  $\alpha$  we obtain

$$\alpha = \frac{1 - \left[ \frac{R_o (1 + 2/3 r) - 1}{\lambda} \right]^2}{1 - r^2}$$

For normal incidence (as implied by the subscript o) and low incident energies, it is reasonable to set  $\lambda$  equal to 2/3. The values of  $\alpha$  calculated from the entries in Table II are plotted in Figure 34.

The scatter is considerably greater than in the past, however, it is clear that contamination causes significant changes in  $\alpha$  for both gold and aluminum. Except for the interactions with the contaminated aluminum, the  $\alpha$  values appear to be remarkably independent of source temperature.

The consistency of previous argon (clean) gold results makes this interaction a logical reference point for the evaluation of the present data. At ambient temperature, the values of  $\alpha$  reported here differ very little from earlier results (indicated by the broken line, Figure 34). However, with increasing source temperature,  $T_s$ , the two sets of data diverge rapidly. This behavior suggests that the surface may have been rougher than those generated in the past. Since the initial gold surface was deposited in a bell jar at  $10^{-5}$  torr, there is the possibility that the resulting structure might differ from those laid down in the cryogenic environment at  $10^{-10}$  torr. As we have noted in past reports, any roughening of the surface has a profound effect on  $\alpha$ , both in magnitude as well as the slope,  $\Delta\alpha/\Delta T_s$ . In any event, the accommodation coefficient for argon is decidedly greater (for contaminated gold). On the other hand, the  $N_2$ -Au results are very puzzling in that they exhibit very little sensitivity to contamination level. One conjecture is that the effect of contamination on  $\alpha$  is masked by surface topology. But why this should be more effective for nitrogen than argon is an open question.

The results of the rough surface measurements are listed in Table III. The thermal accommodation coefficients for argon (assuming diffuse reflections) range from 0.848 to 0.989 for the two source temperatures.

It is not the actual value of  $\alpha$  which is important but rather there is a significant departure from unity for these rough, contaminated surfaces. This is contrary to the general assumption that such surfaces should be fully accommodating. Similar behavior has also been noted for the interaction of argon and krypton with a rough silver surface.

Concerning Figure 10 we have no explanation for the functional differences between the Kr and Ar curves, in particular why the Kr curve should have a negative curvature. The fact that the magnitude of  $\alpha$  is greater for Kr than Ar is significant in itself and is in accord with previous data. On the basis of these and all previous data, certain general statements can be made for gold targets, i. e., :

1. Even at relatively low incident energies  $\alpha$  and  $\sigma_{\perp}$  are substantially less than unity.
2. Both  $\alpha$  and  $\sigma_{\perp}$  are strongly influenced by temperature. The nature of the dependence is not clear especially since the surface structure is unknown.
3. For a given source temperature, the magnitudes of the normal momentum and thermal accommodation coefficients both increase with the molecular weight of the incident particles.
4. From the measured values of  $R_{\theta}$ , it is apparent that the flux distribution of scattered particles cannot have a cosine distribution. This follows from the fact that, on the average, the scattered particles leave the surface in a direction forward of the surface normal.
5. The above behavior becomes more pronounced at greater angle of incidence and with higher incident particle velocities.
6. The assumption sometimes introduced in theoretical treatments that the tangential momentum component is preserved is not valid at these low energies. Such an assumption is completely incompatible with all data so far obtained.

Thermal accommodation versus temperature calculations based from the data given in Figure 11 are given in Figure 35.

The  $\alpha$ -temperature relationships thus determined exhibit a puzzling feature for both argon and krypton, namely they both increase monotonically with temperature. In general, current

theories predict that  $\alpha$  should first decrease with temperature and then pass through a minimum before rising. Such has been the behavior with gold as described in our previous reports.

From simple geometrical considerations it is possible to construct a model which can account for the rising  $\alpha$ -temperature behavior. Assume that the other surface has cross sections of the type suggested in Figure 36. The surface of an individual grain is taken to be flat but the boundaries consist of trenches (A) and/or sudden changes in elevation (B), each being associated with sloping sides. From results obtained from gold surfaces, we have learned that with increasing incident velocity the spatial distribution of the reflected particles becomes lobular and the average flux vector moves away from the surface normal. Referring back to Figure 36, we see that a certain fraction of the scattered flux from an element of the incident beam will be intercepted by an adjacent wall. The particles undergoing one local encounter\* will be associated with some energy accommodation,  $\alpha$ . Those striking the adjacent wall will rebound with an effective coefficient  $\alpha^1 = 1 - (1 - \alpha)^2$ . Thus, to a first approximation, the net accommodation coefficient is  $\alpha^* = \alpha (1 - f_1) + f_1 \alpha^1$  where  $f_1$  is the fraction undergoing a second collision with a neighboring surface. According to this model, as the incident velocity increases a larger fraction will make a second collision so that  $f_1$  will increase. Although  $\alpha$  may decrease with incident energy according to theory, it is still possible for  $f_1$  to increase rapidly enough to mask this effect. Thus  $\alpha^* = \alpha (1 - f_1) + f_1 [1 - (1 - \alpha)^2]$  can increase monotonically. This purely phenomenological argument is advanced to illustrate that a reasonable explanation of the gross behavior is possible without resorting to basic atomic interaction details.

The thermal accommodation coefficients (see Figure 37) calculated for normal incidence from Figure 11 exhibit the same characteristics noted in previous experiments. The reproducibility of both the krypton and argon data establishes confidence in the experimental procedure and provides a convenient reference. The flux data presented in Figures 16 through 33 will not be commented upon individually, however, certain general observations may be made, i.e.:

1. Lobular patterns are observed in the principal plane.
2. These are found to be sensitive to incident particle energy and to the age of the surface.
3. The force measurements are consistent with the scattering data.
4. In many cases the flux distribution for normal incidence departs from a cosine relationship. The observed flattening could account for values of  $R_o$  being less than unity.

The significance of the results tabulated for rough, contaminated surfaces (Table III) is that it may indeed be very difficult to produce a real surface having unit accommodation, particularly for a wide range of incident particle energy. This has many practical implications, e.g., in the laboratory we must continue to make use of the cavity or momentum trap as a reference measurement.



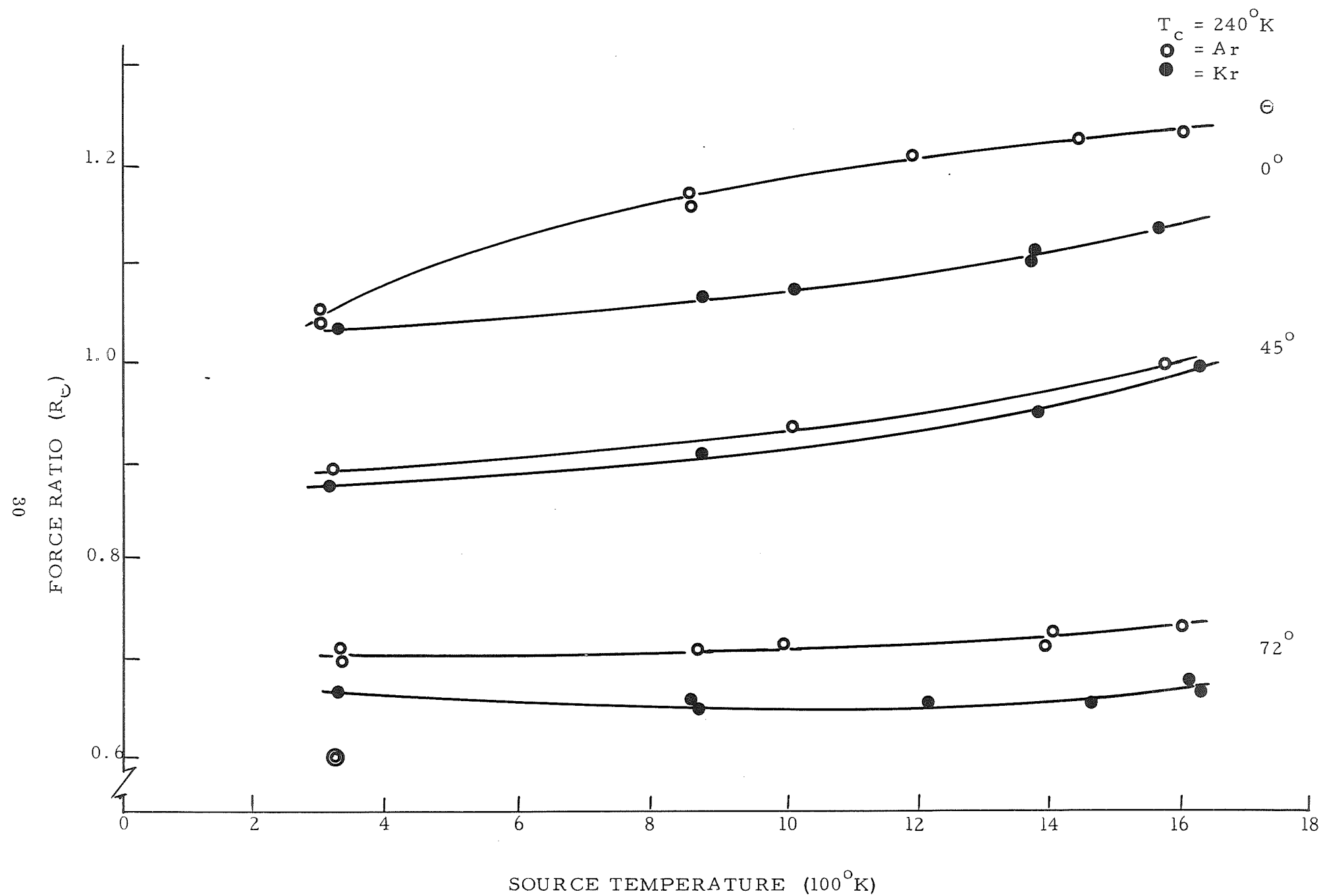


Figure 10

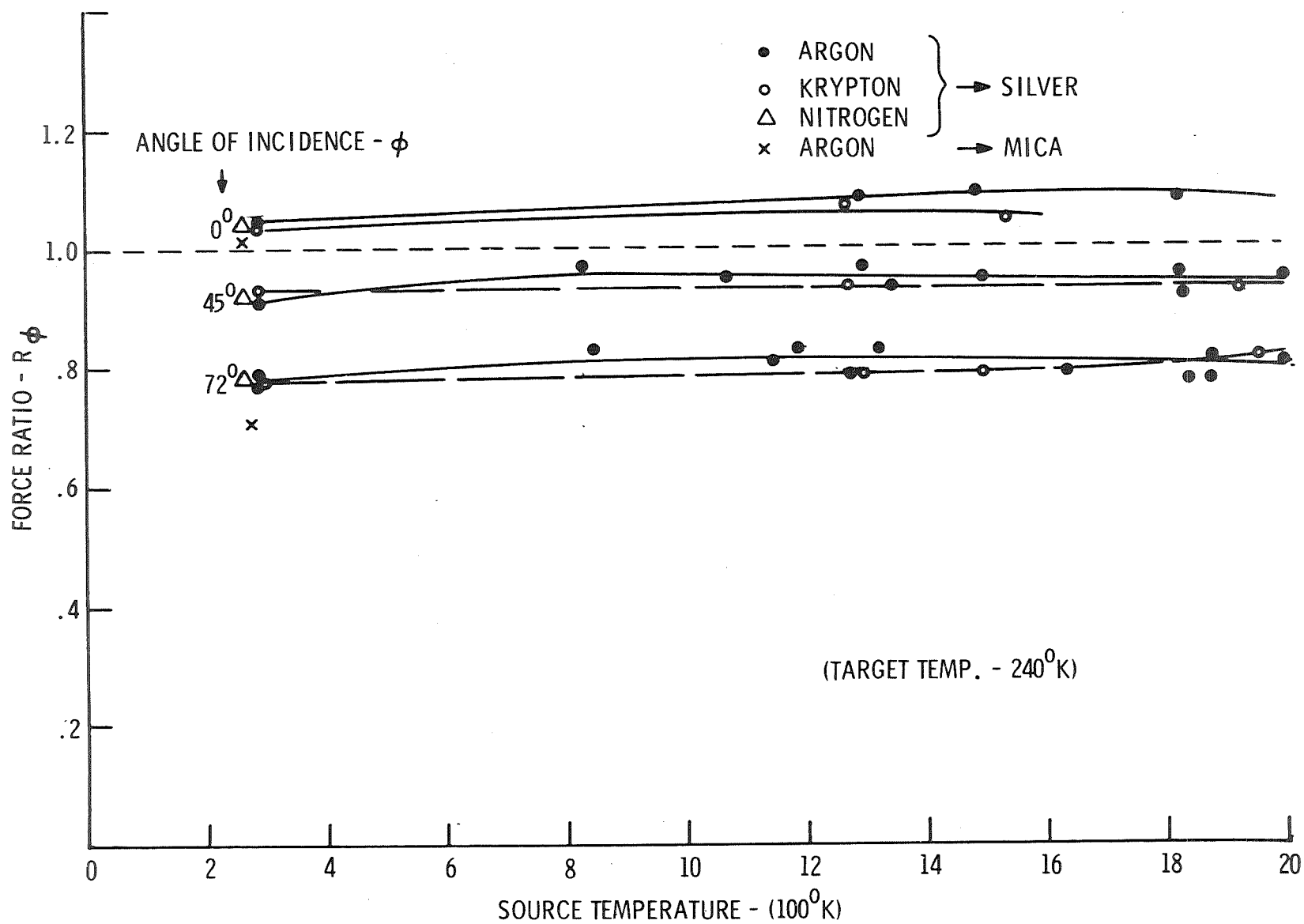


Figure 11

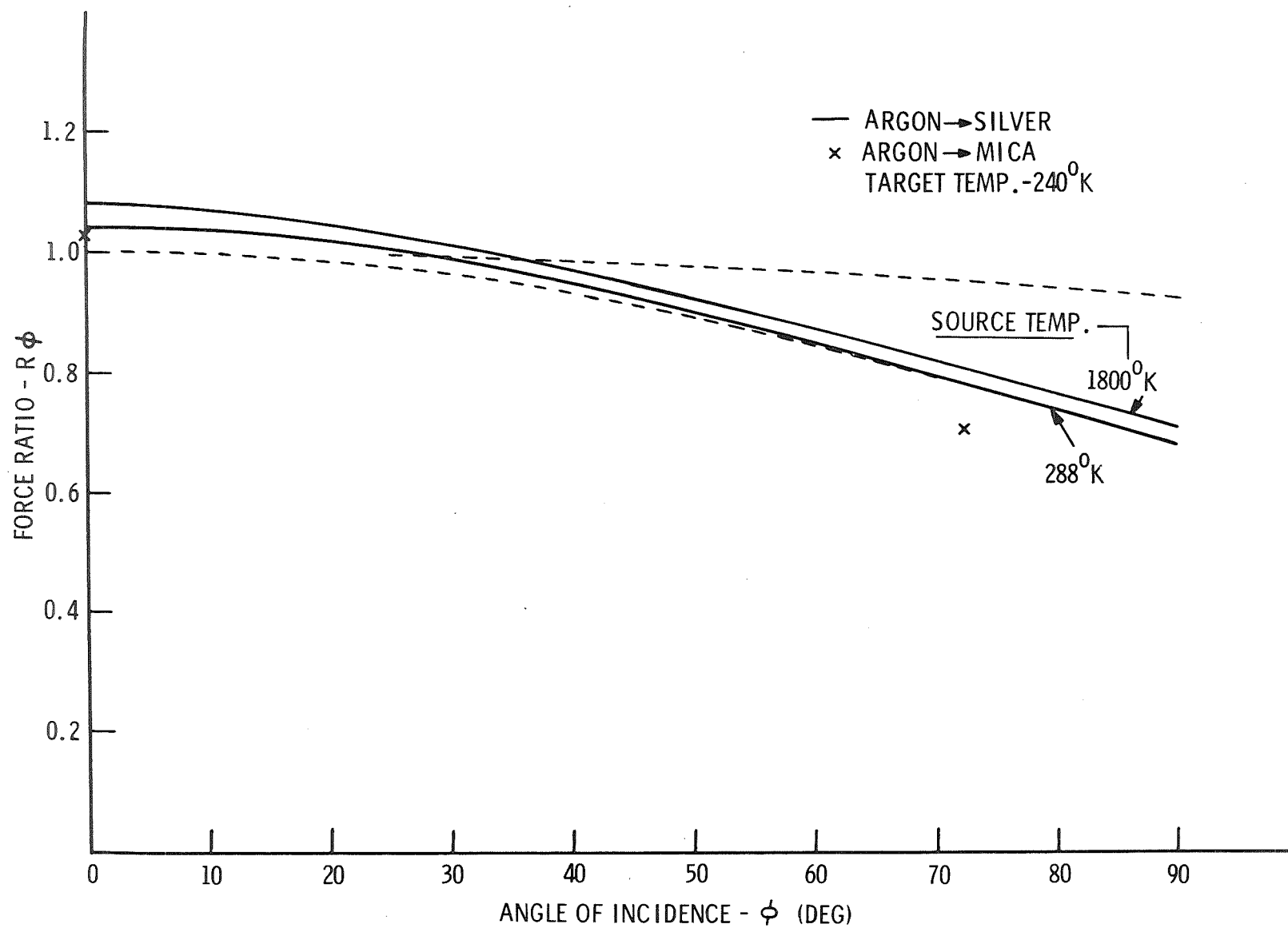


Figure 12

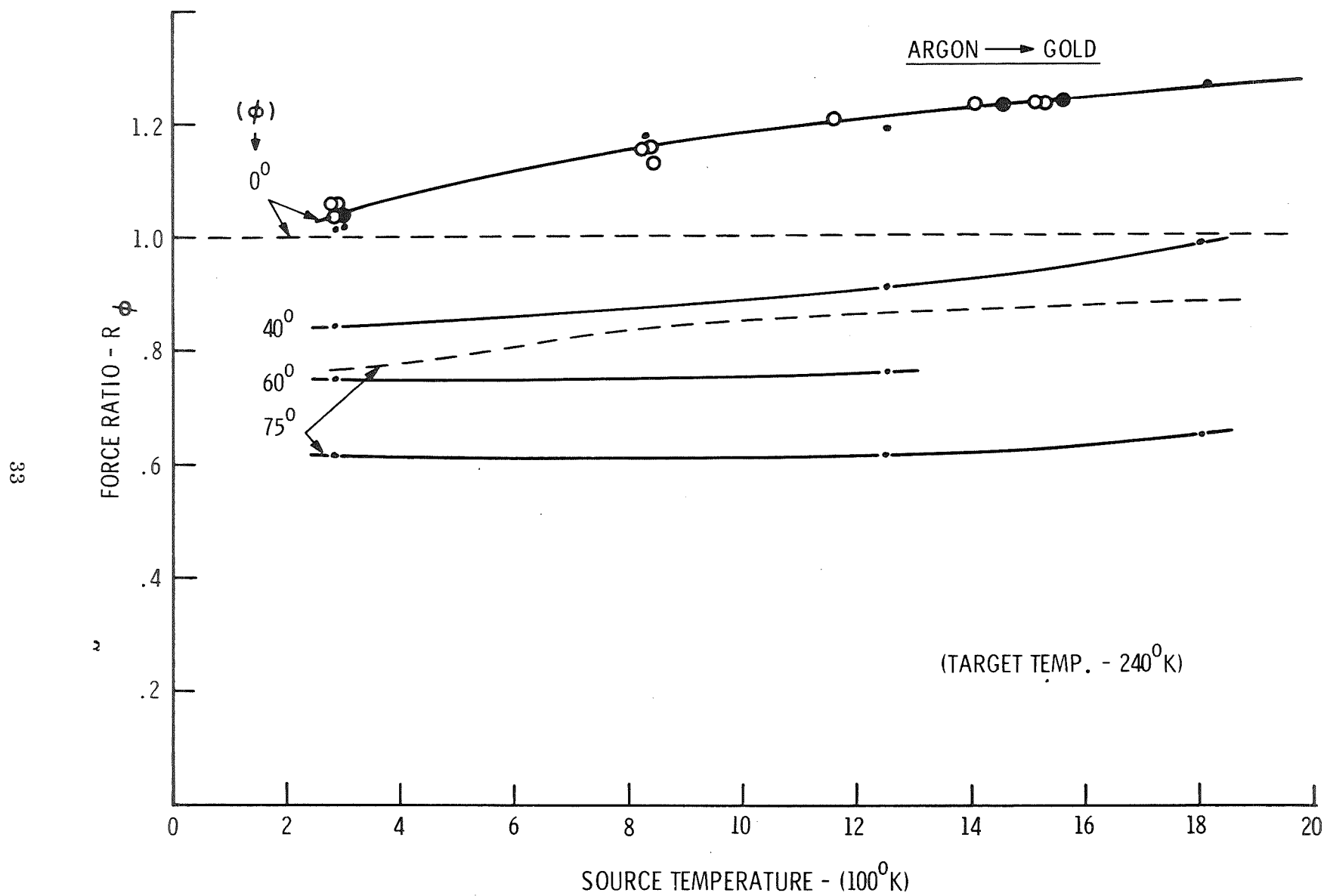


Figure 13

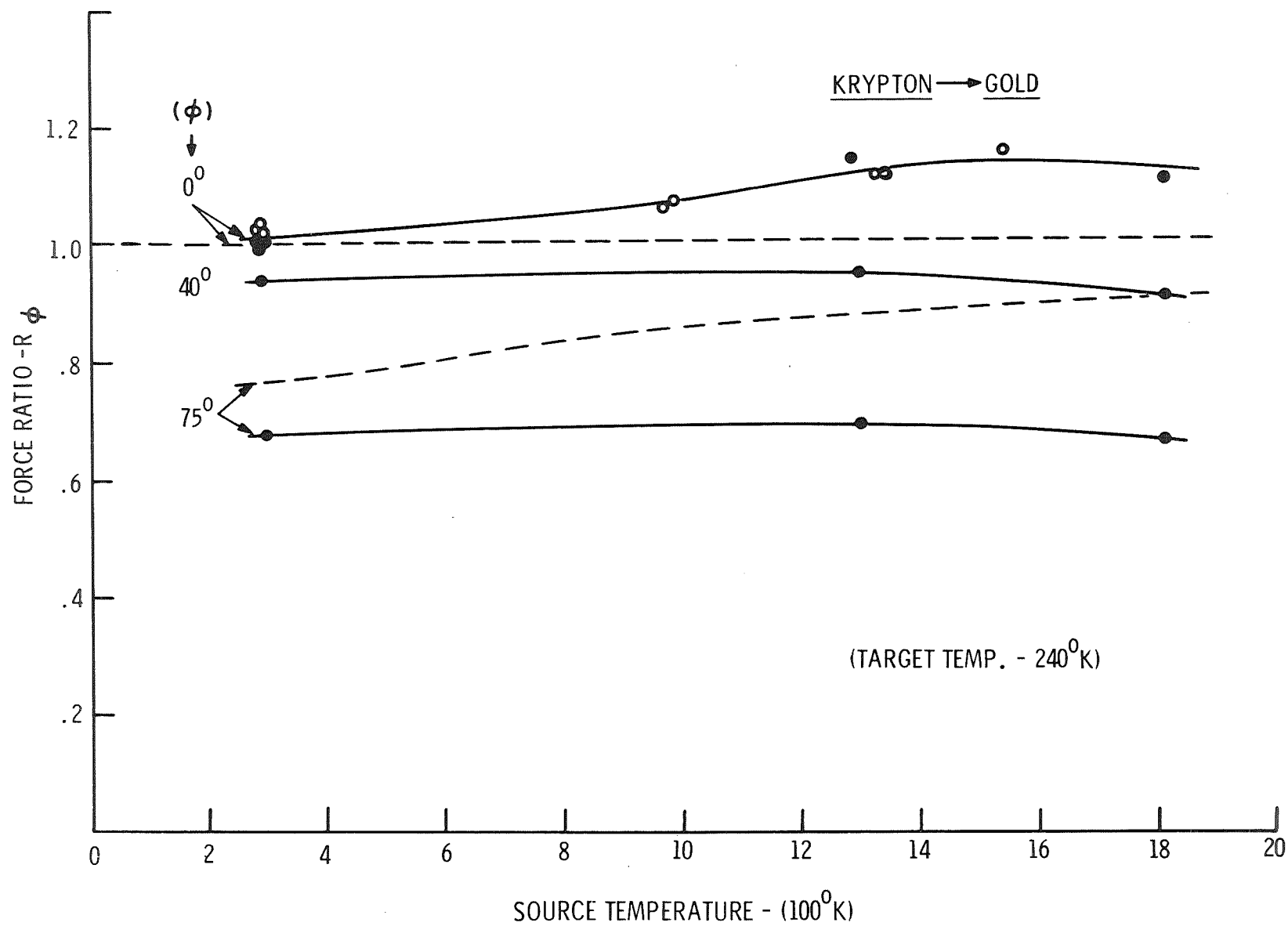


Figure 14

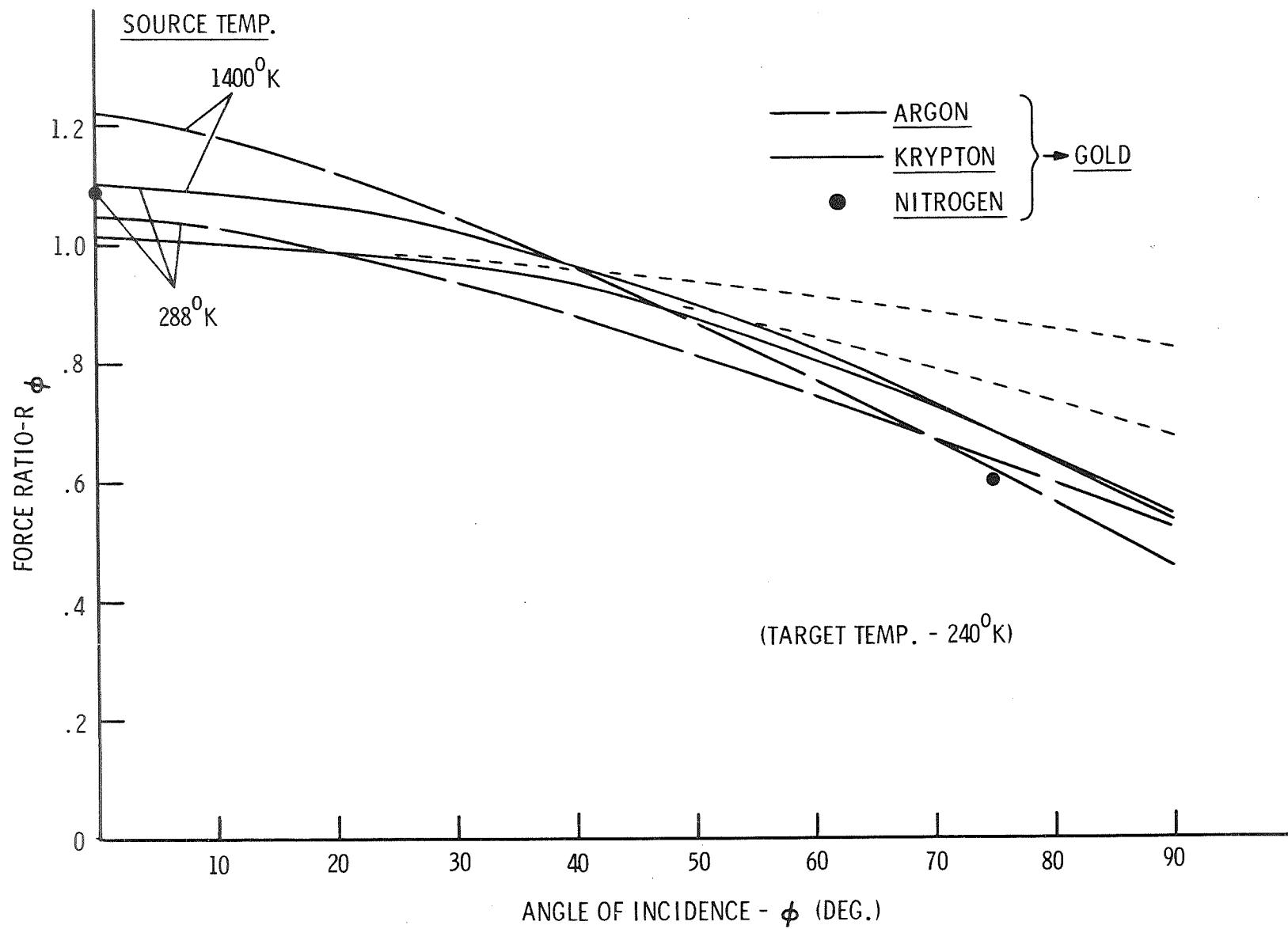


Figure 15

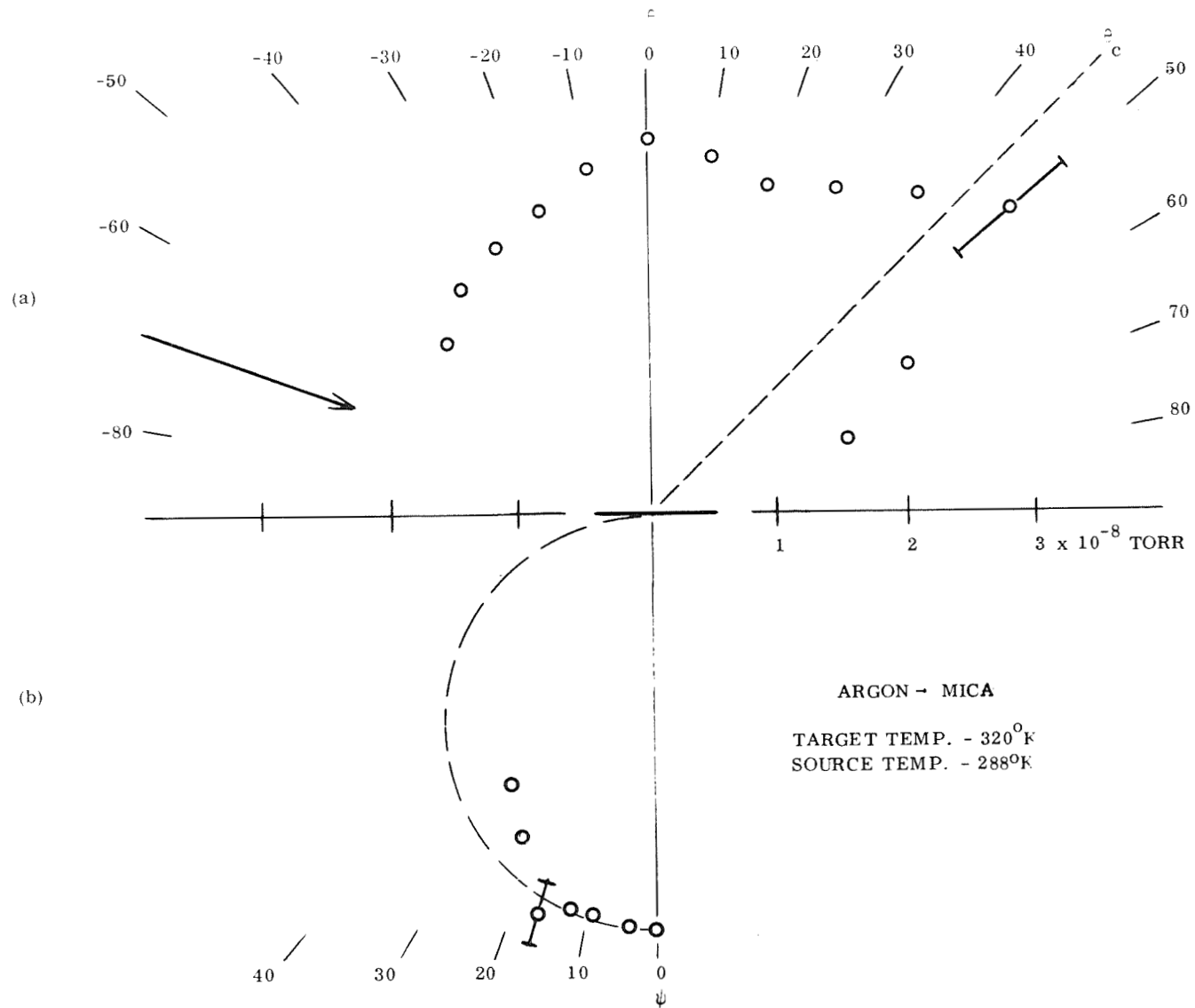


Figure 16

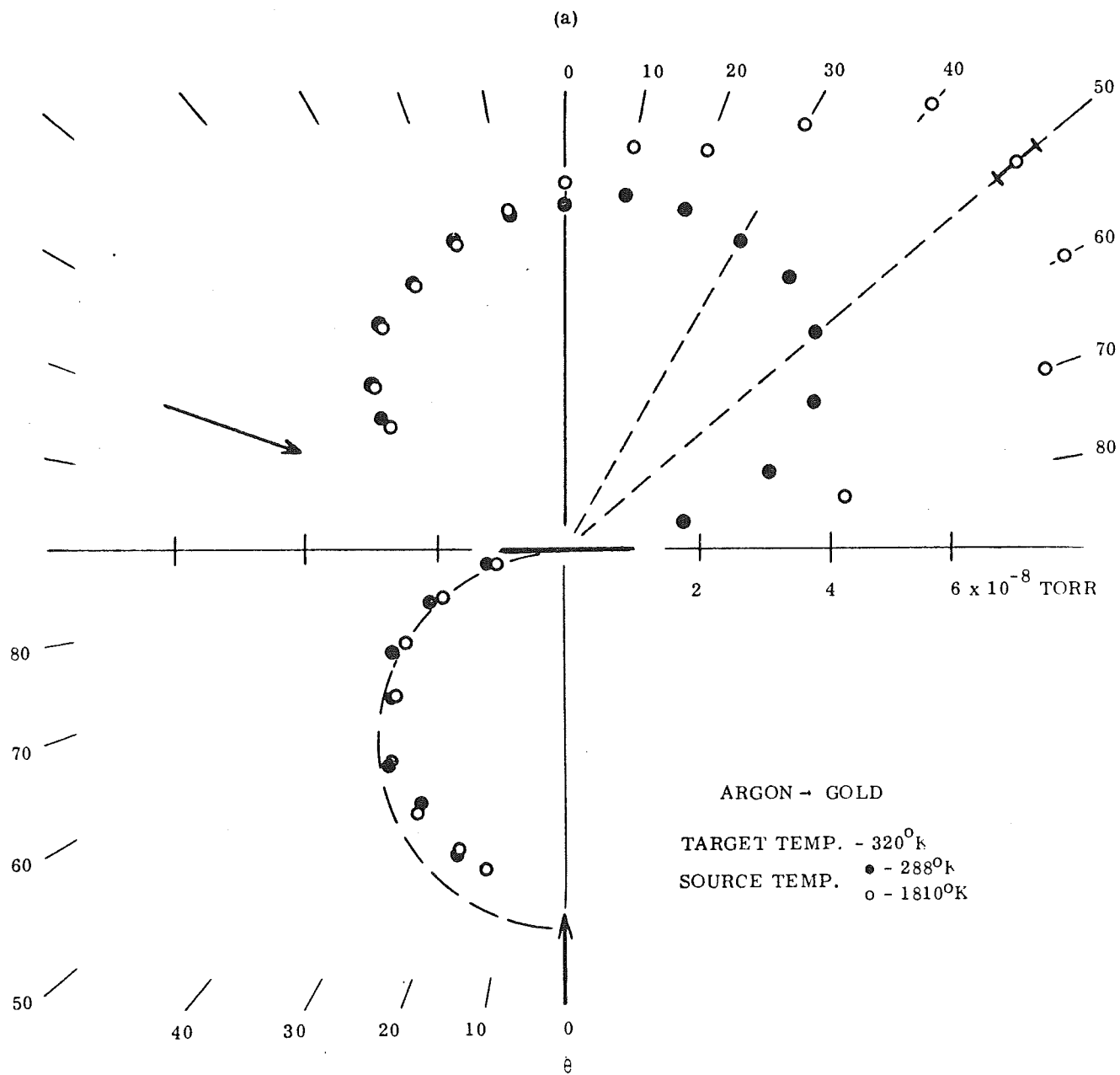


Figure 17



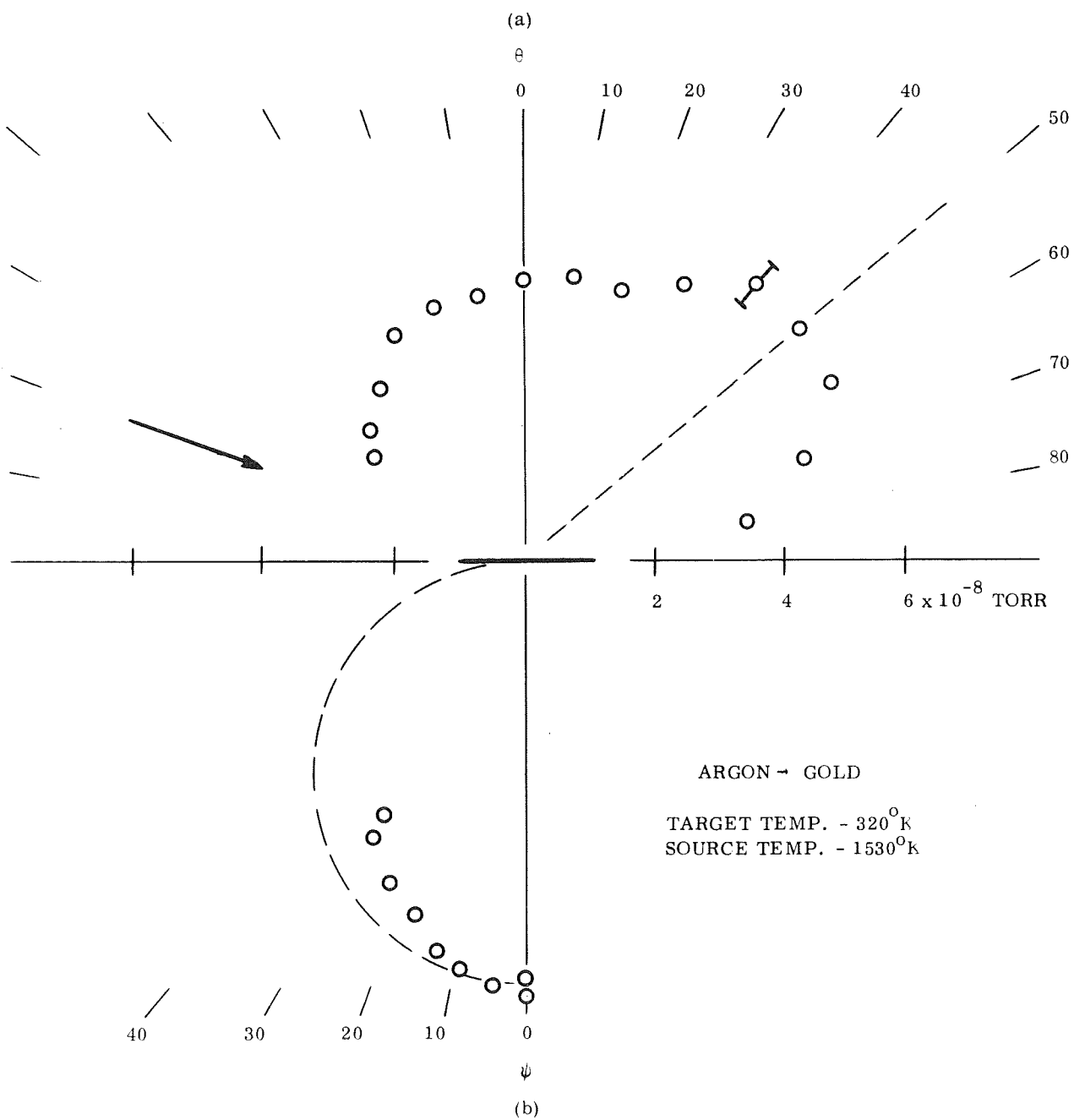


Figure 18

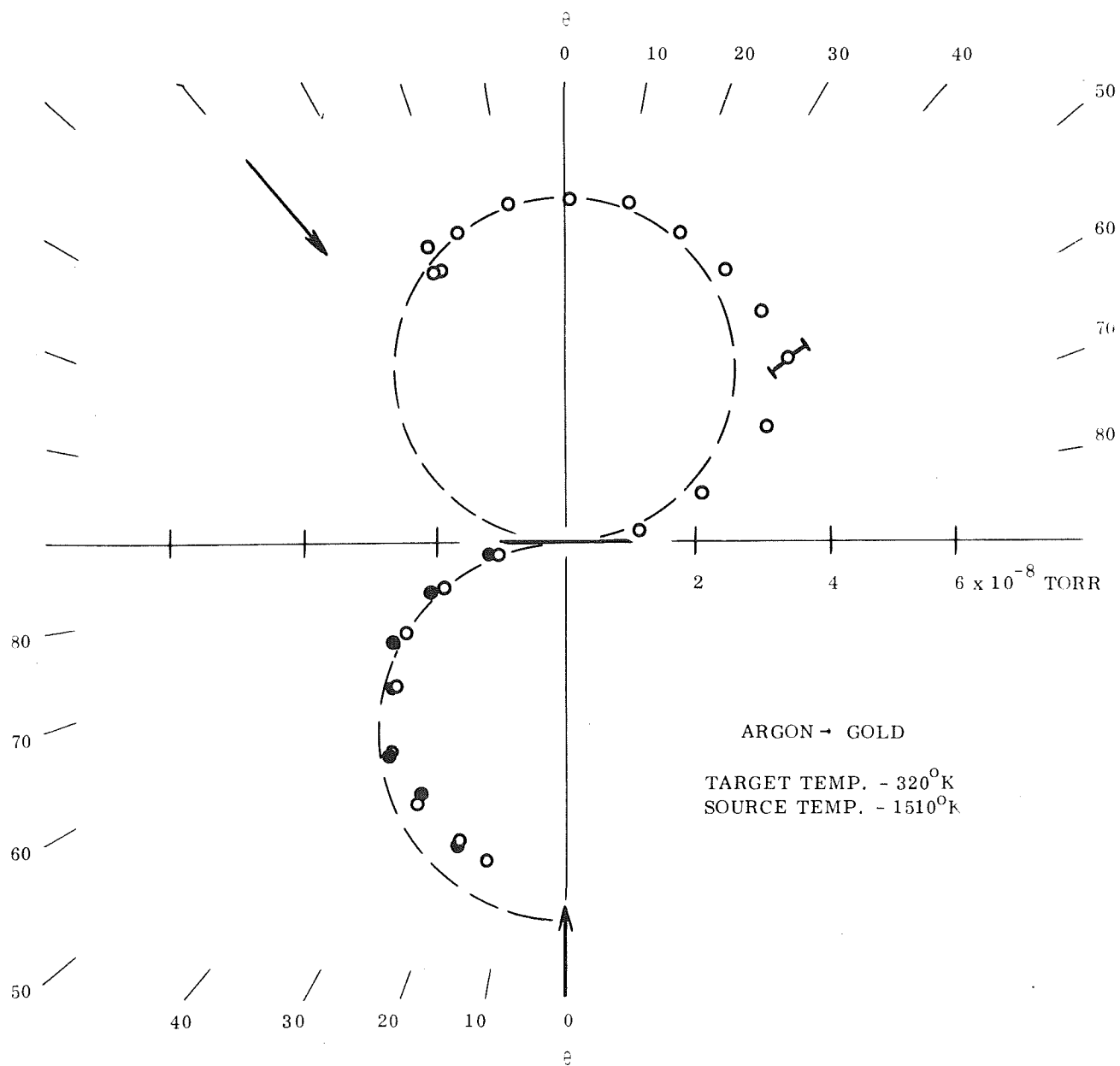


Figure 19

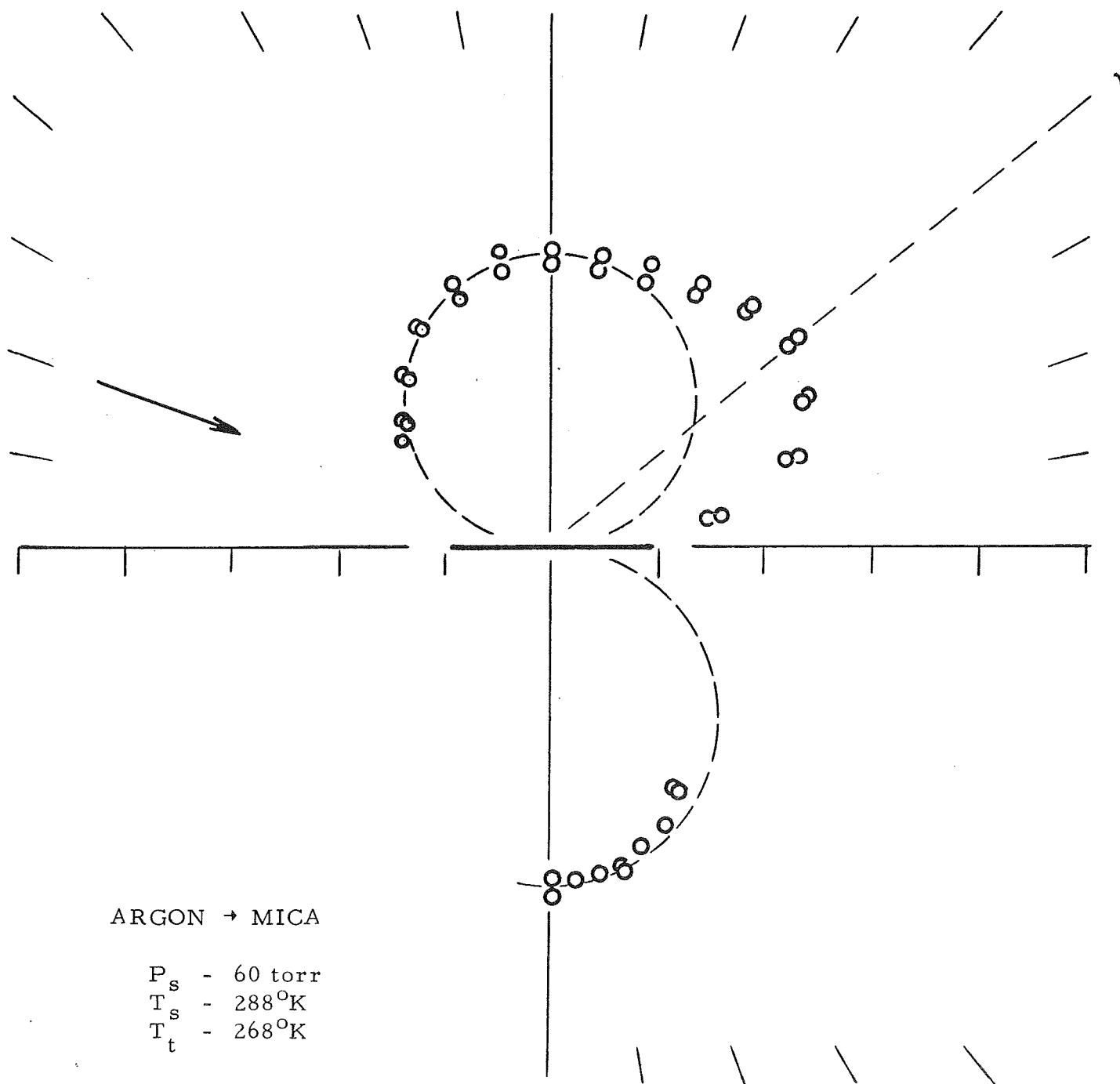


Figure 20

ARGON  $\rightarrow$  MICA

P = 60 torr

T<sup>s</sup> = 332°K

T<sub>t</sub><sup>s</sup> = 268°K

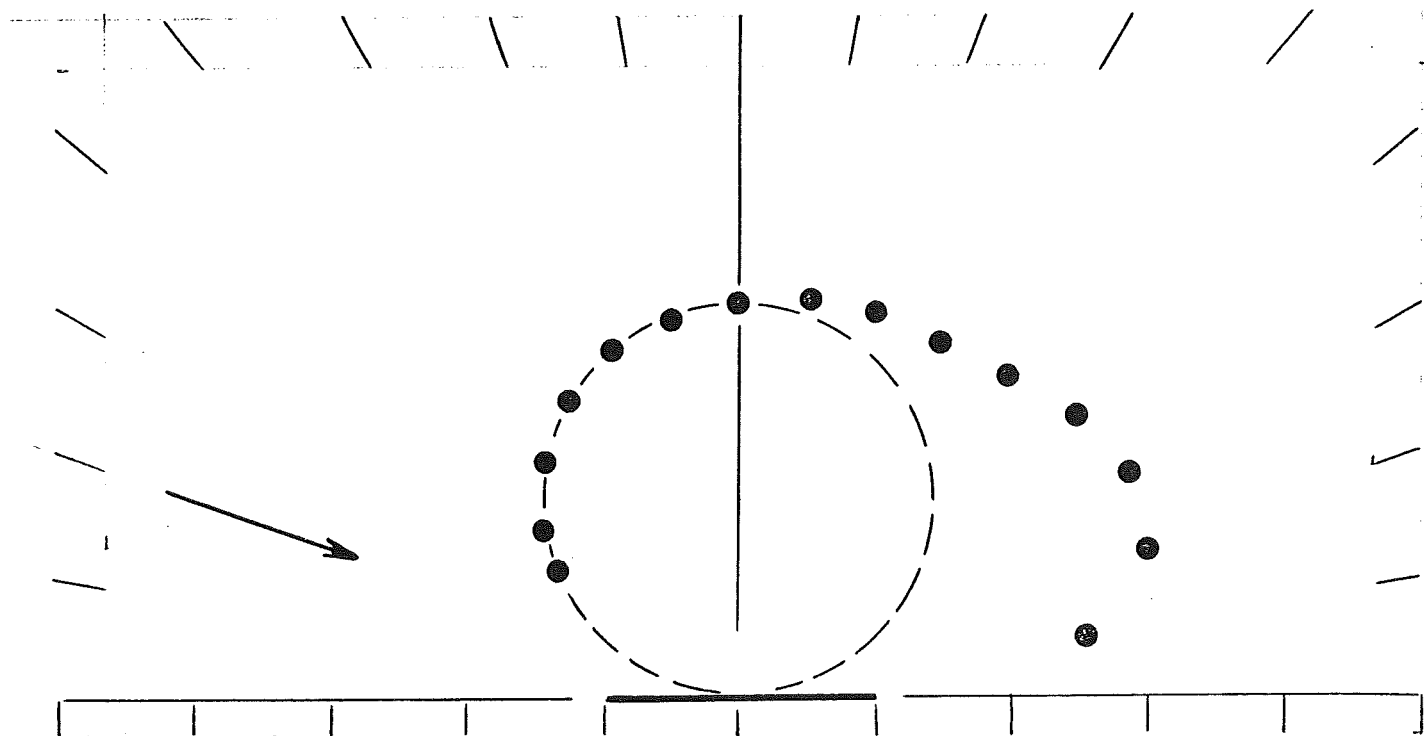


Figure 21

ARGON  $\rightarrow$  MICA

$P = 60$  torr

$T^s = 331^\circ\text{K}$

$T_t^s = 268^\circ\text{K}$

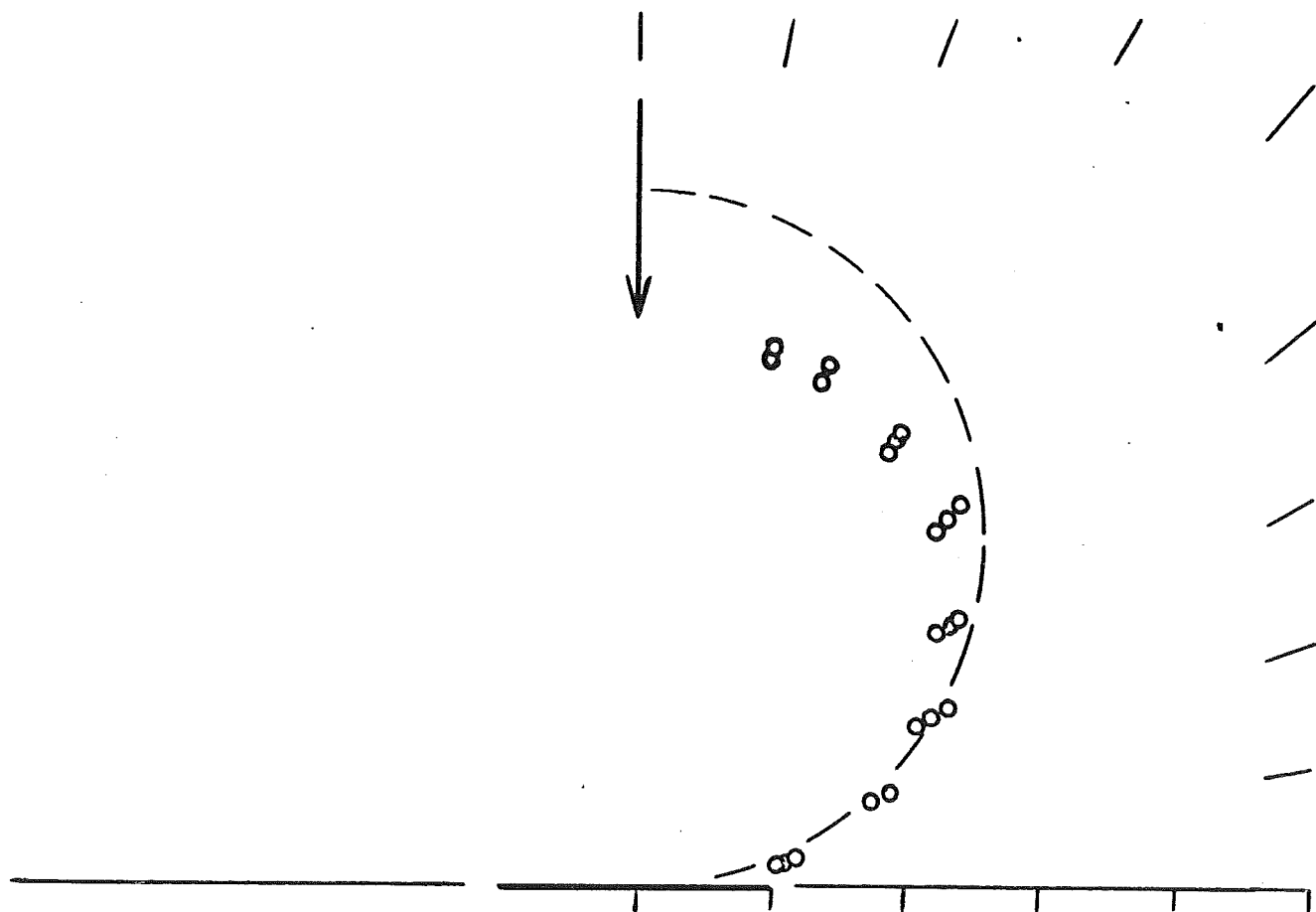


Figure 22

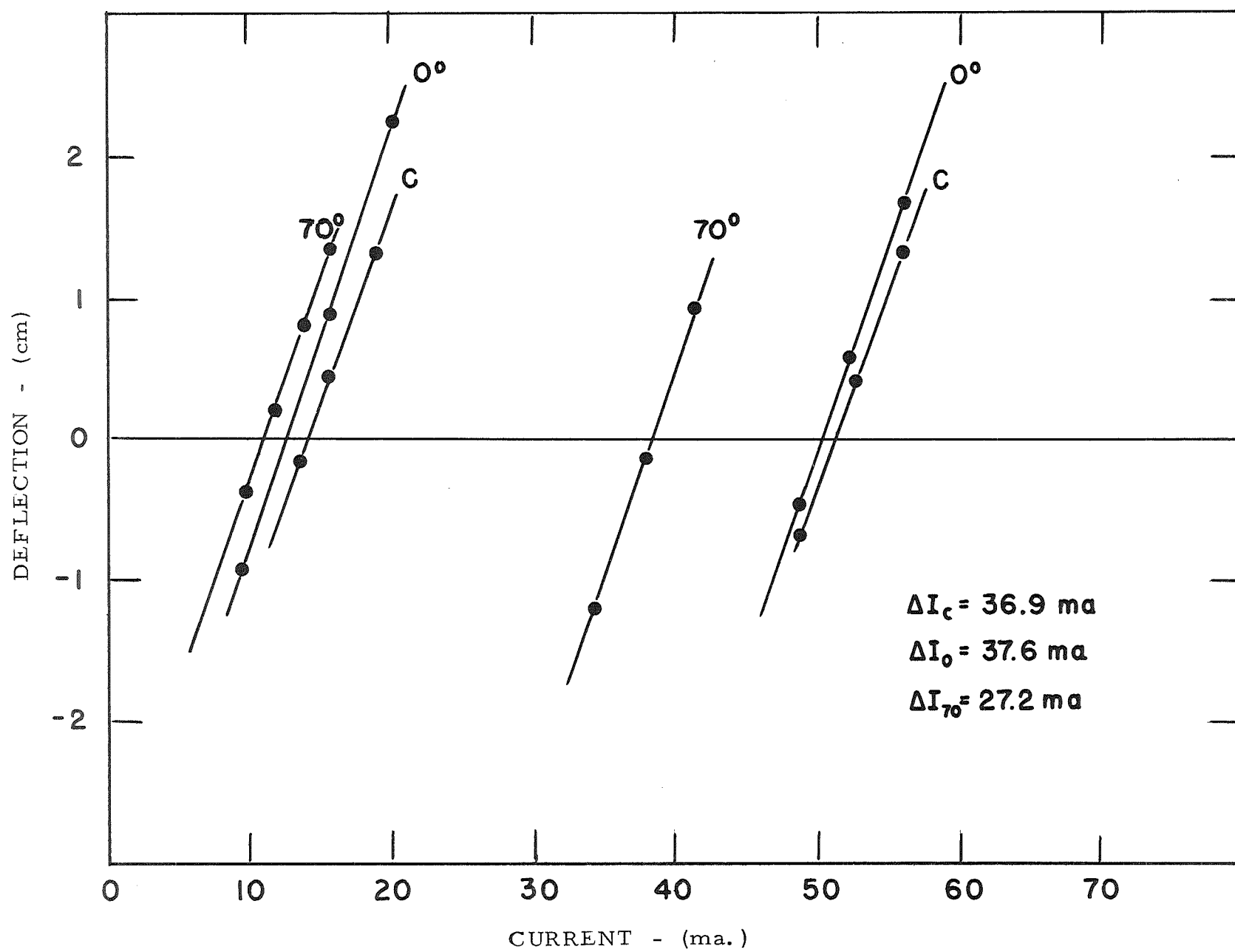


Figure 23

NITROGEN  $\rightarrow$  MICA

$P = 120 \text{ torr}$

$T^s = 289^\circ\text{K}$

$T_t^s = 268^\circ\text{K}$

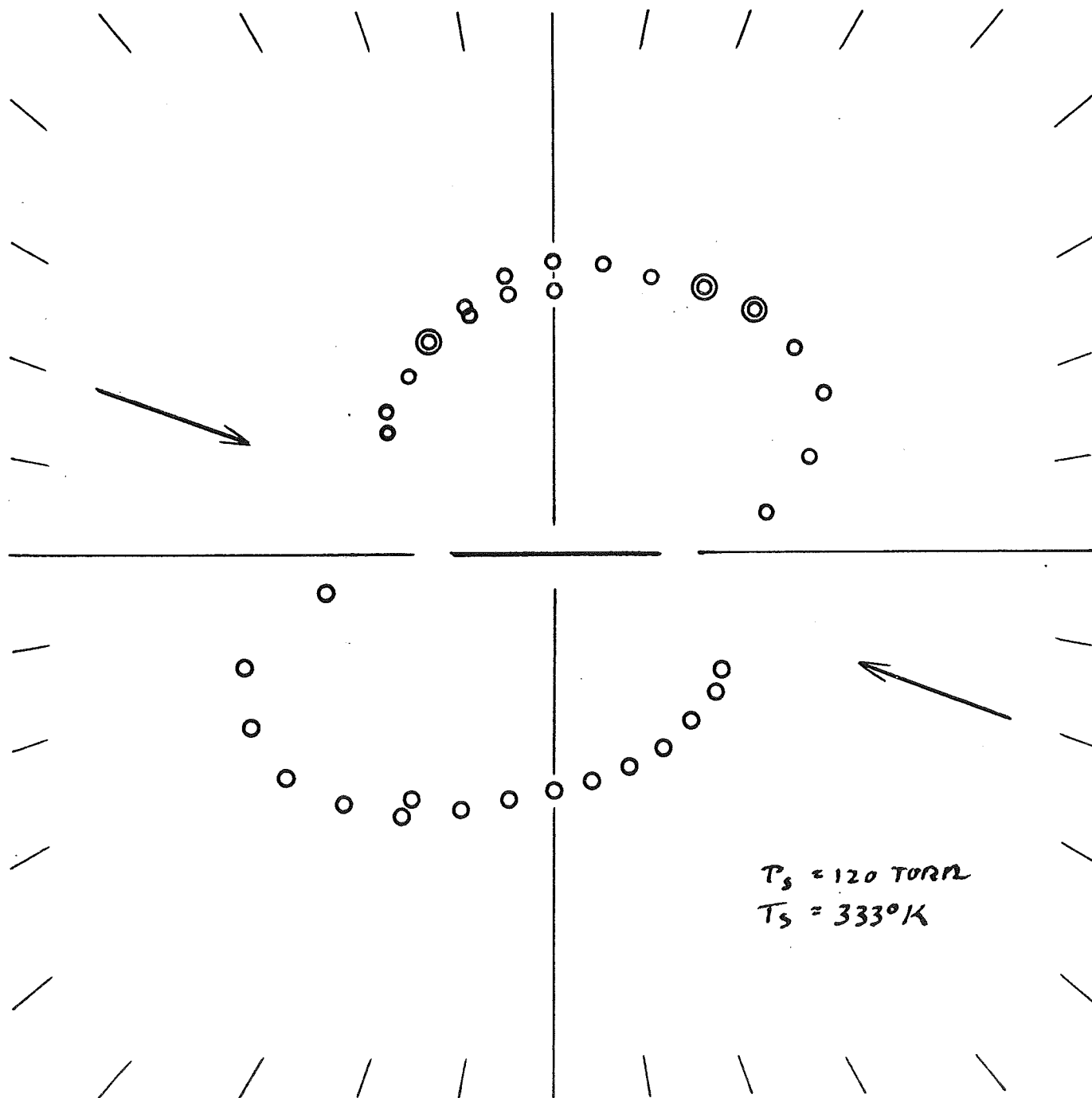


Figure 24

NITROGEN  $\rightarrow$  MICA

P = 120 torr

T<sup>s</sup> = 288°K

T<sub>t</sub><sup>s</sup> = 268°K

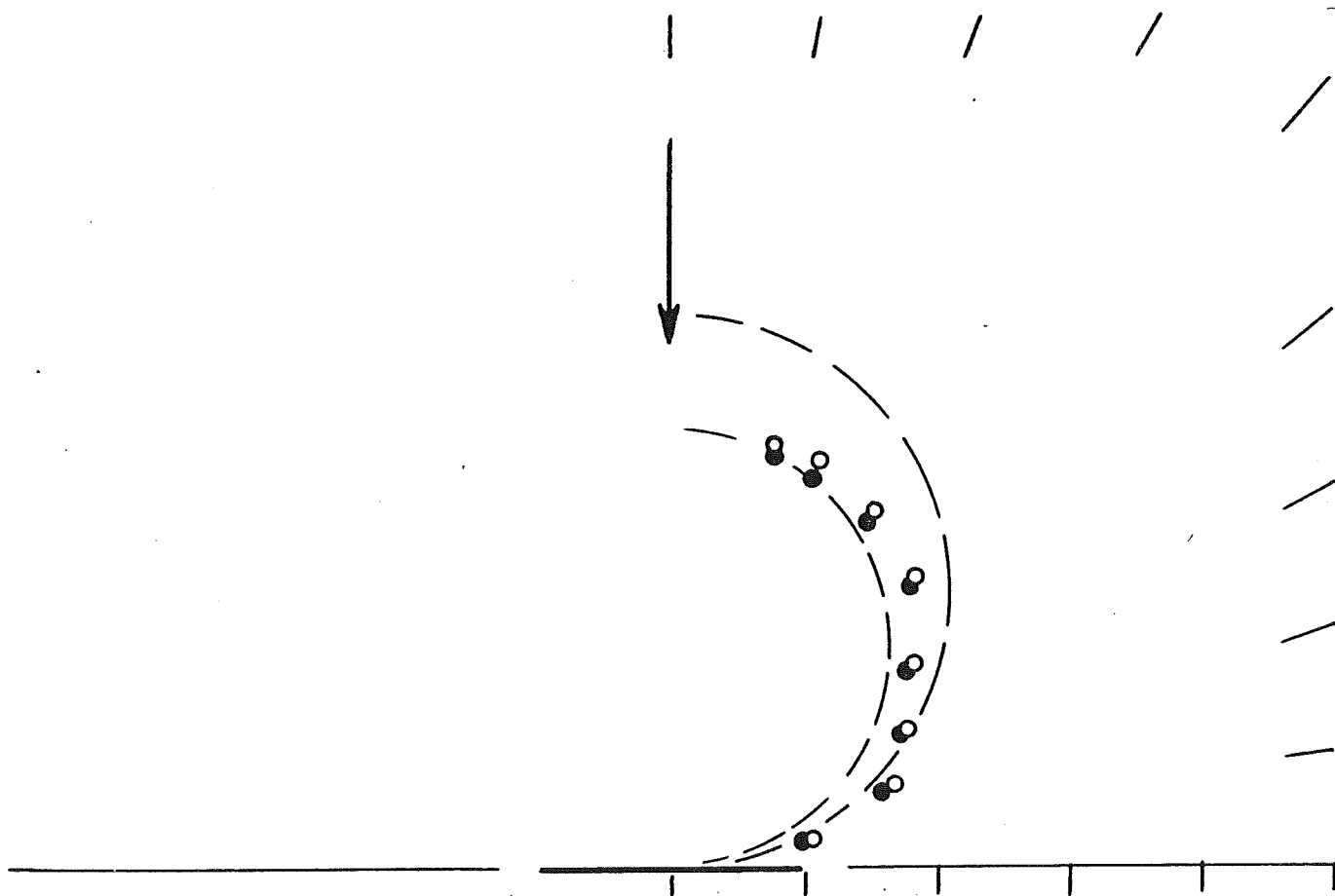


Figure 25



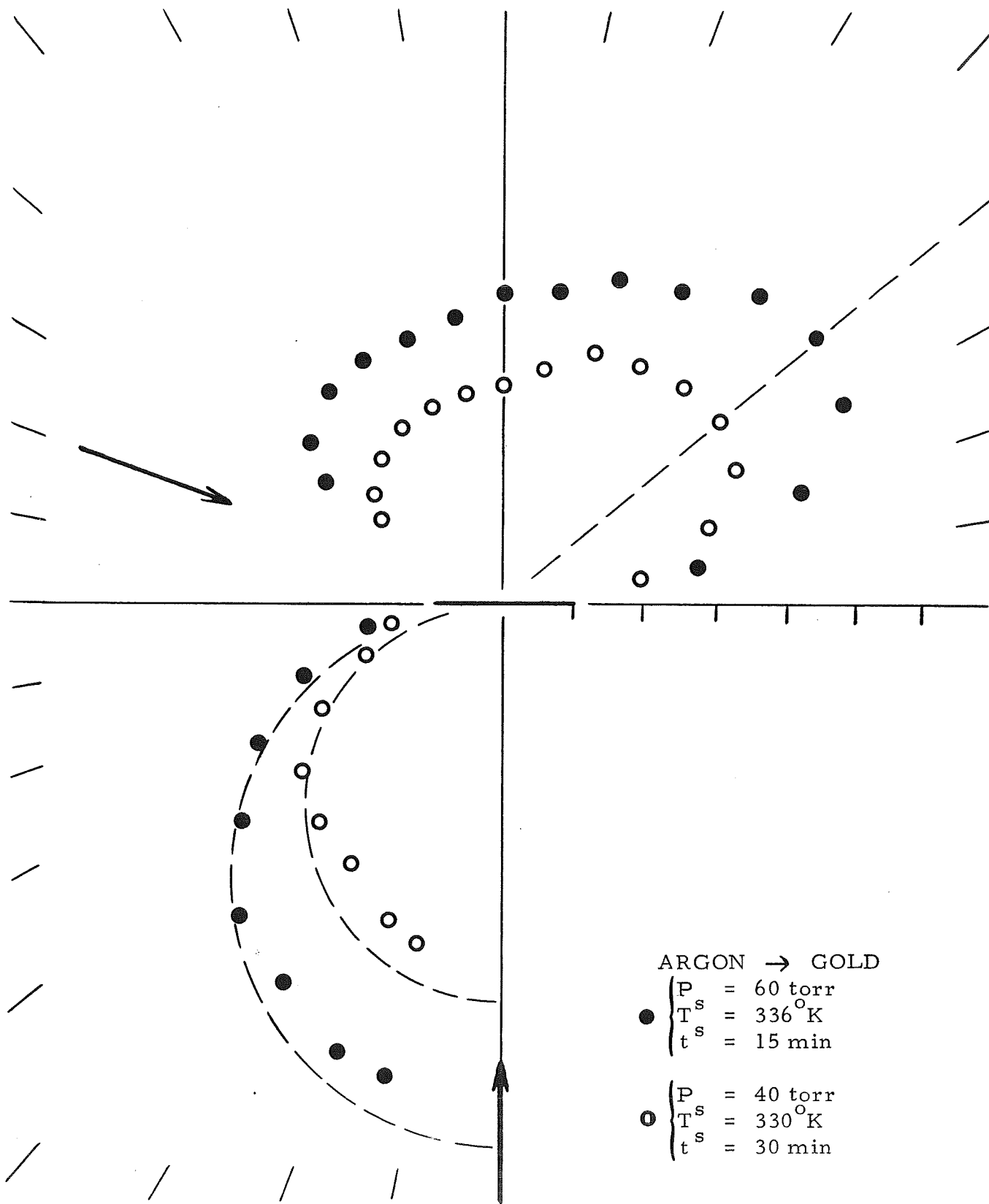


Figure 26

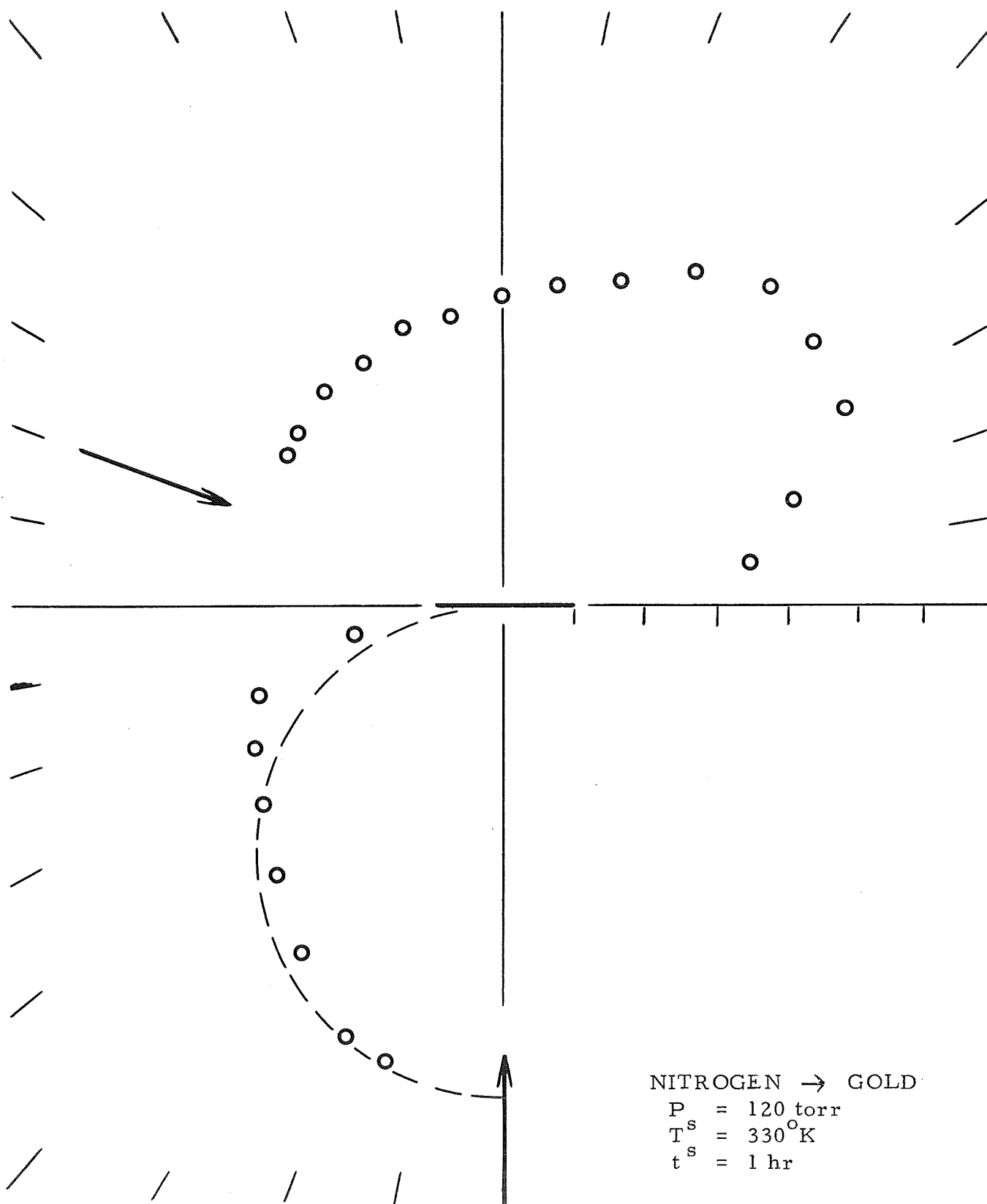


Figure 27

ARGON  $\rightarrow$  GOLD

$P = 60$  torr

$T^s = 290^\circ\text{K}$

$t^s = 21$  hr

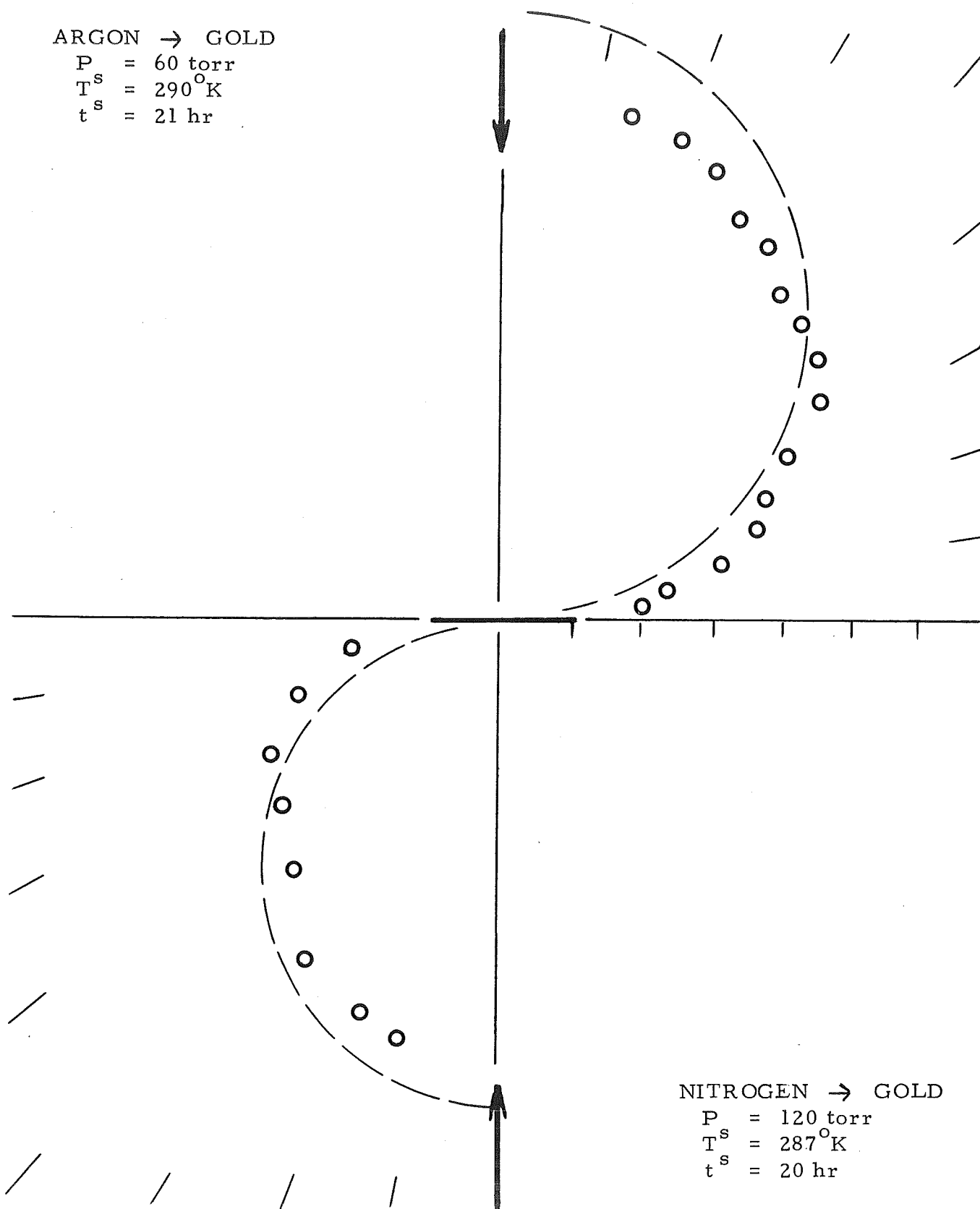


Figure 28

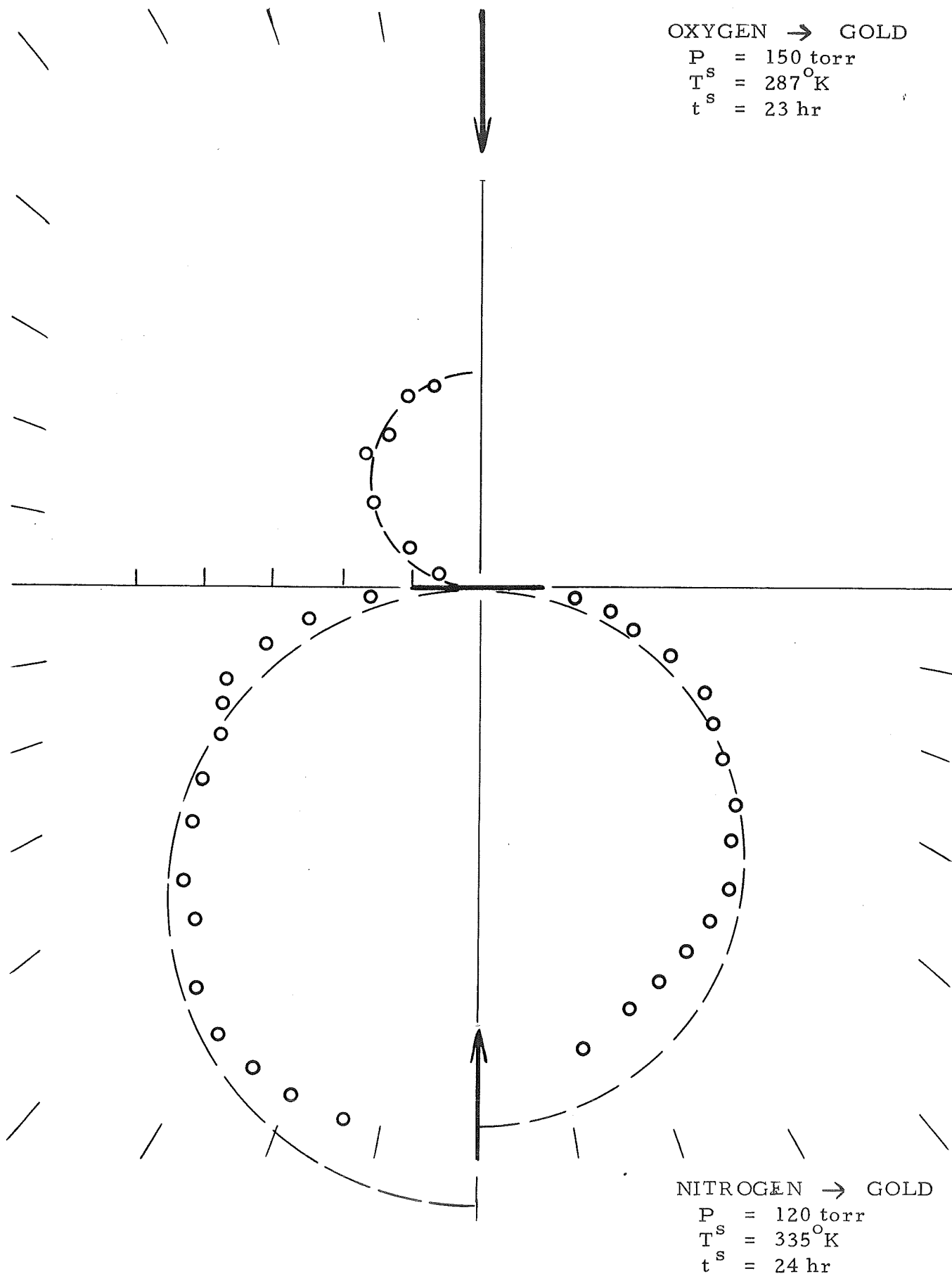


Figure 29

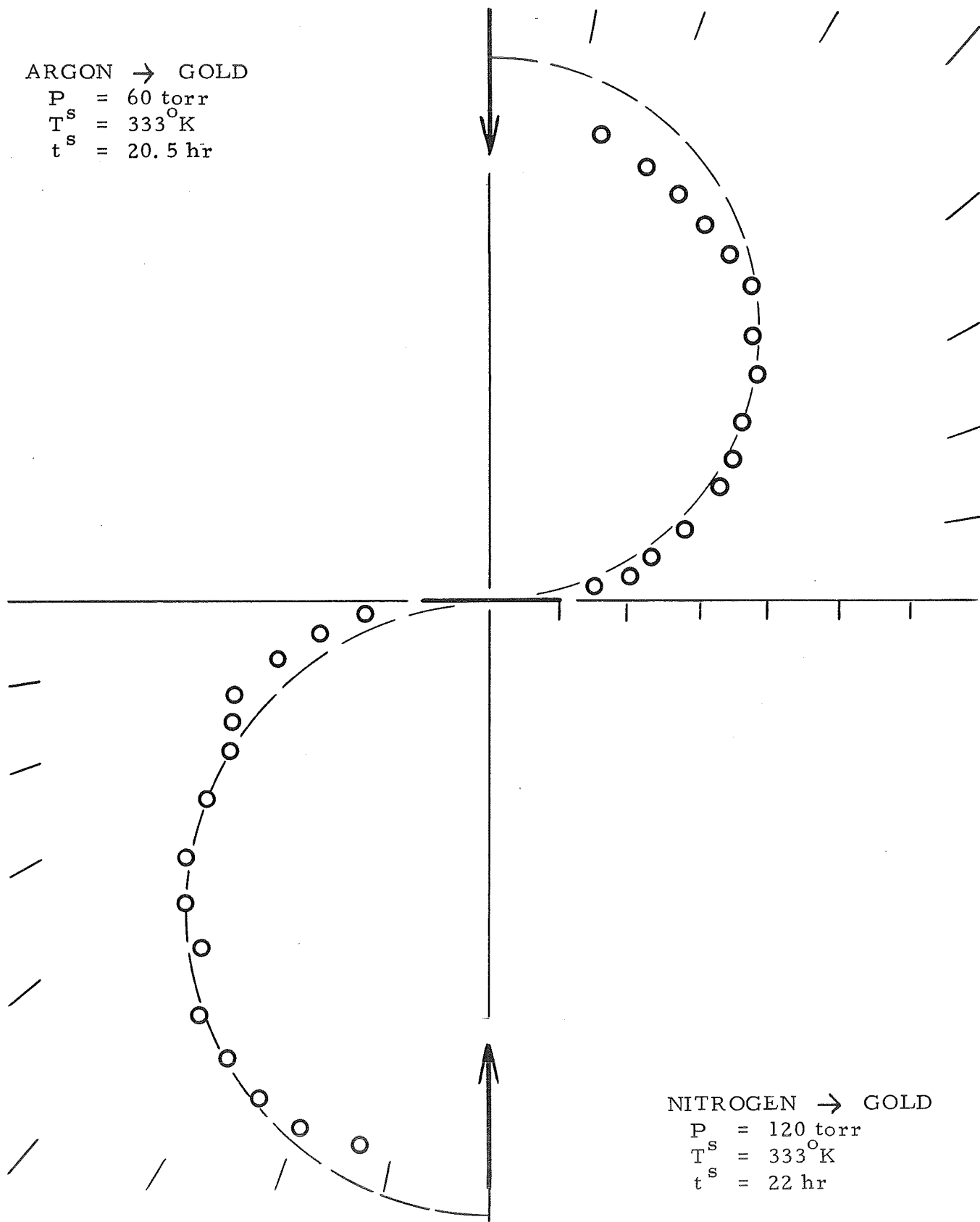


Figure 30  
50

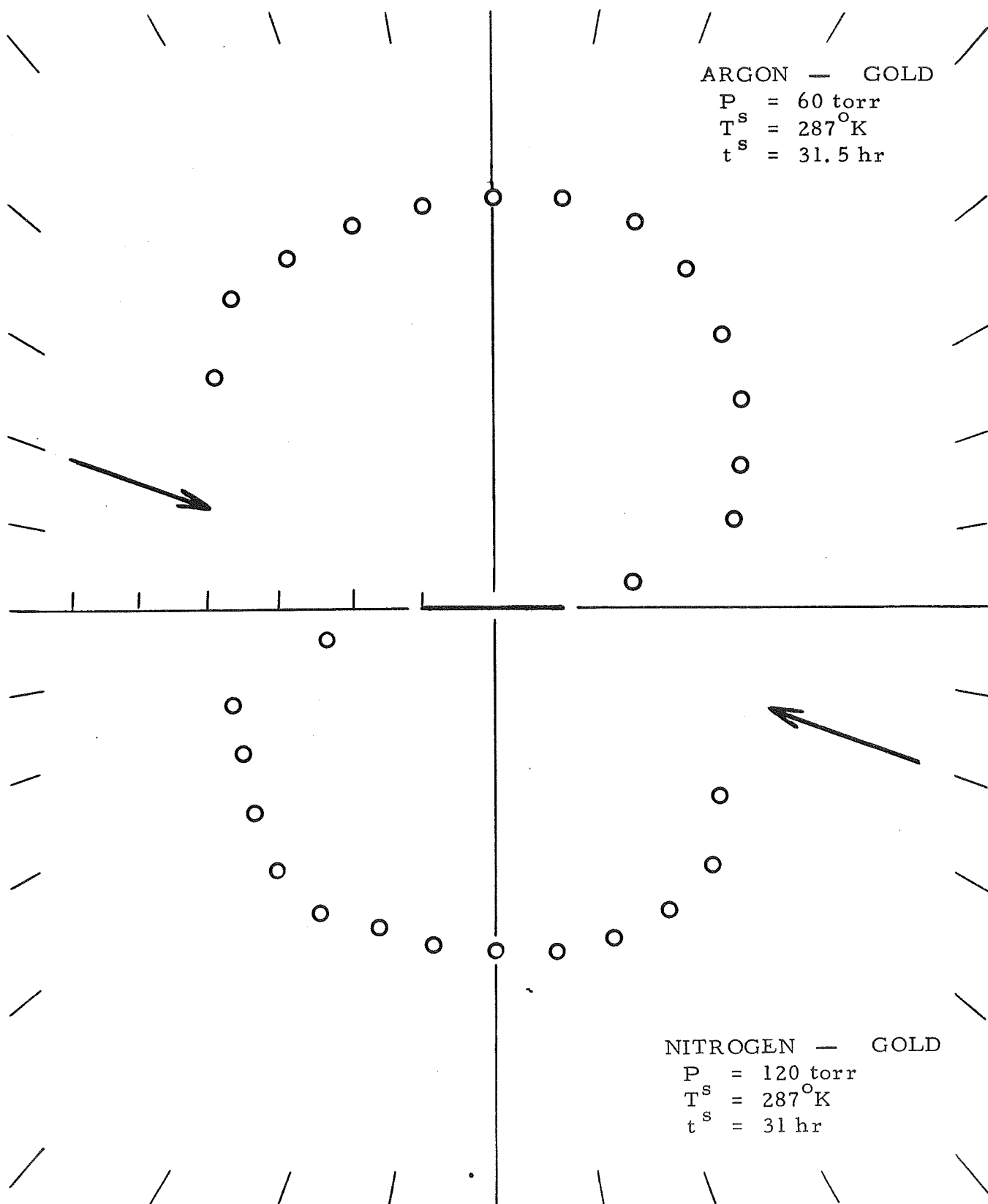


Figure 31

ARGON — GOLD

$P^s = 60 \text{ torr}$

$T^s = 287^\circ\text{K}$

$t^s = 32 \text{ hr}$

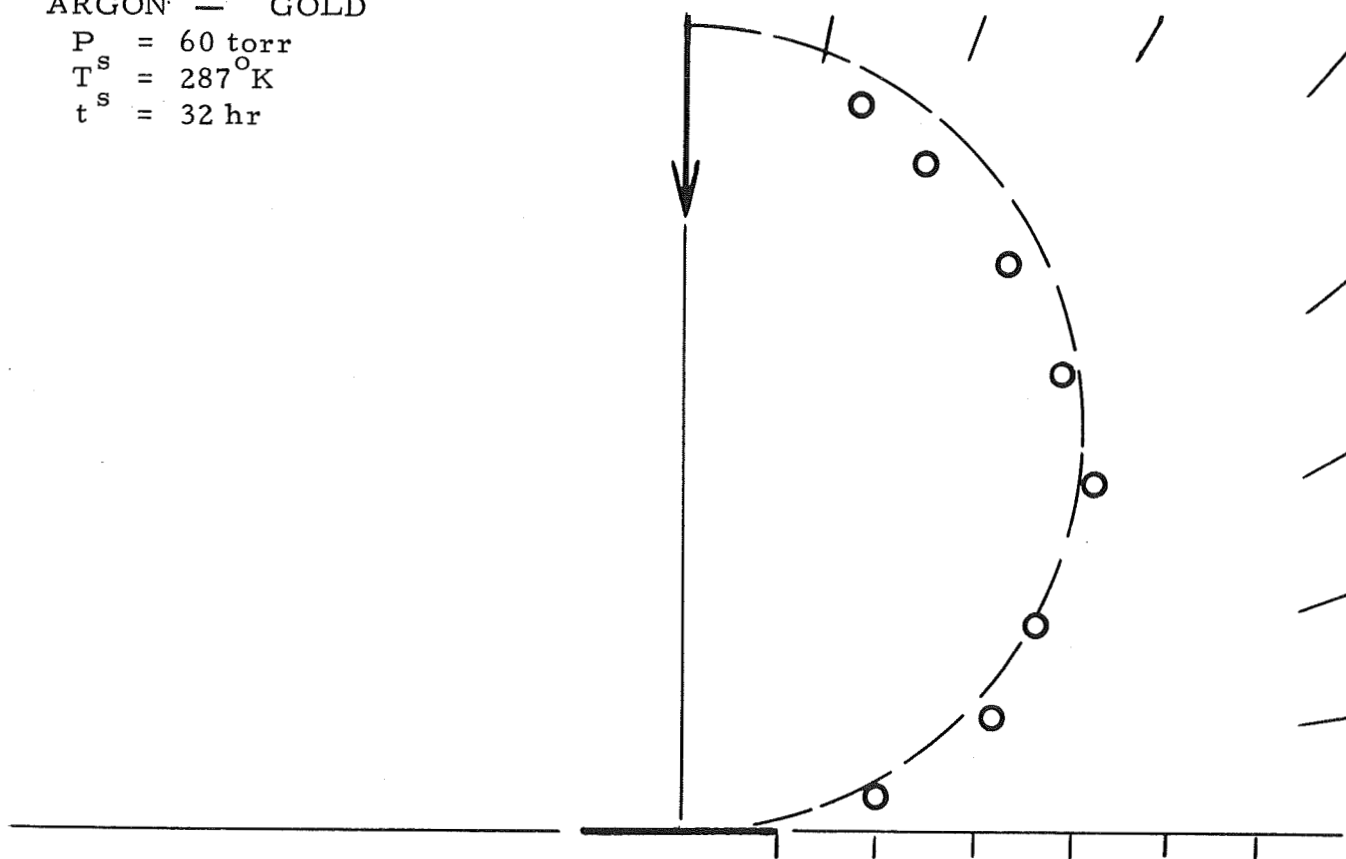


Figure 32

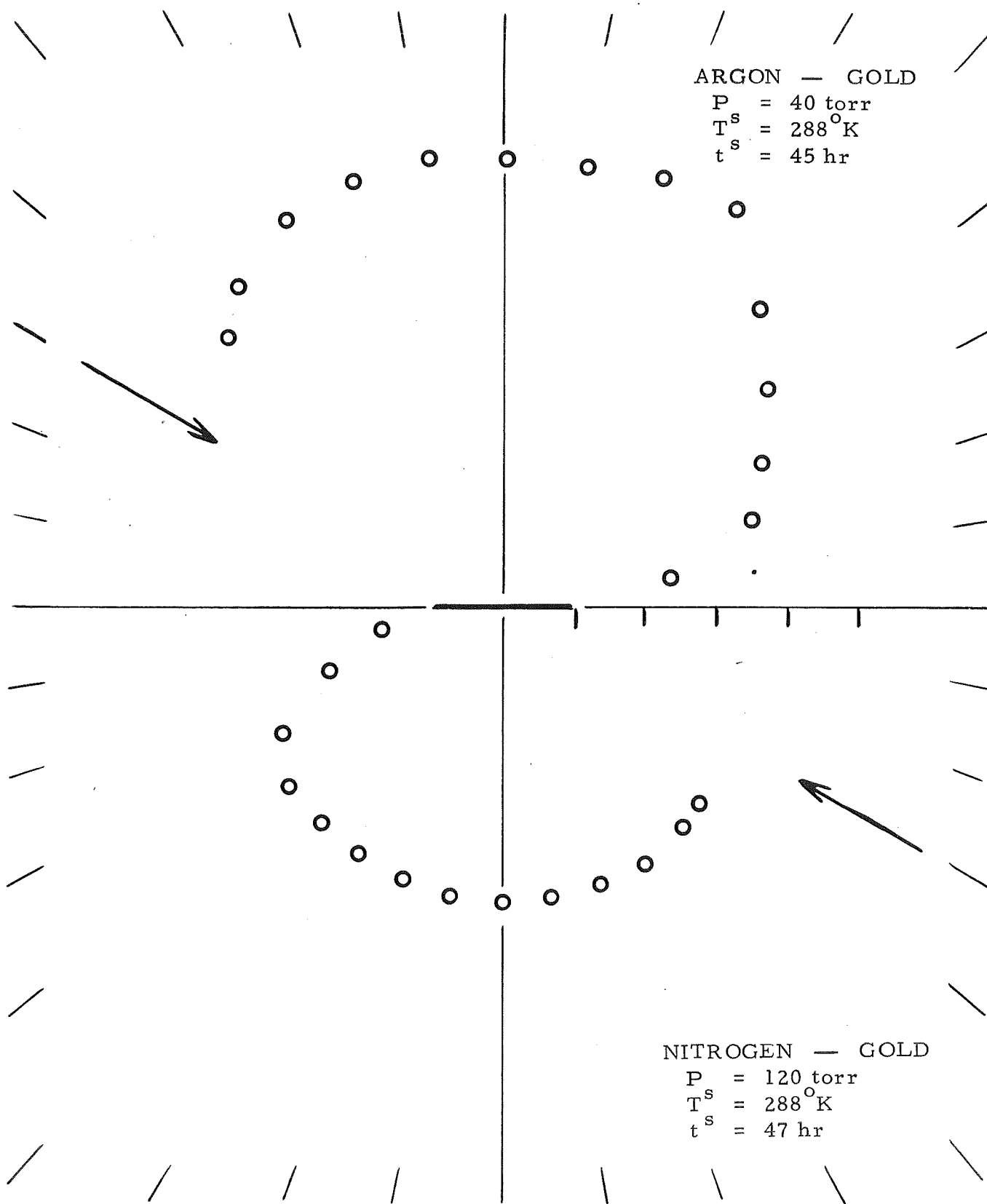
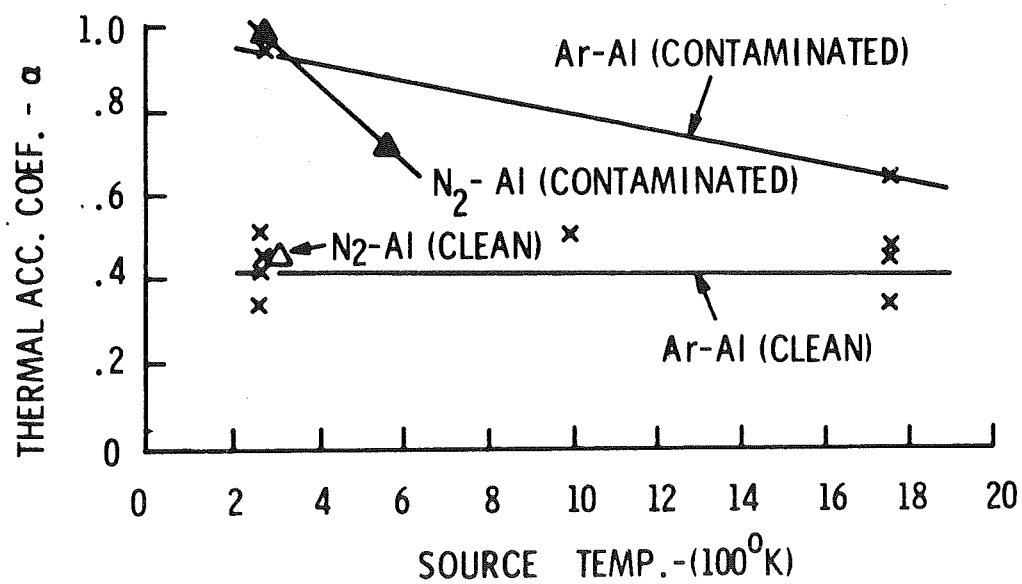
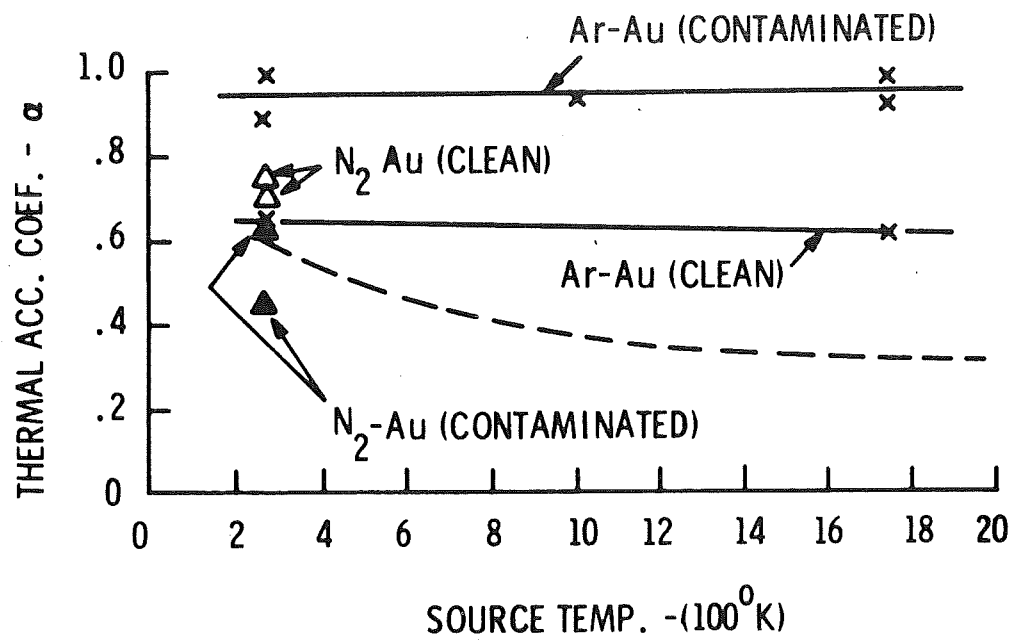


Figure 33





N 103-821

Figure 34

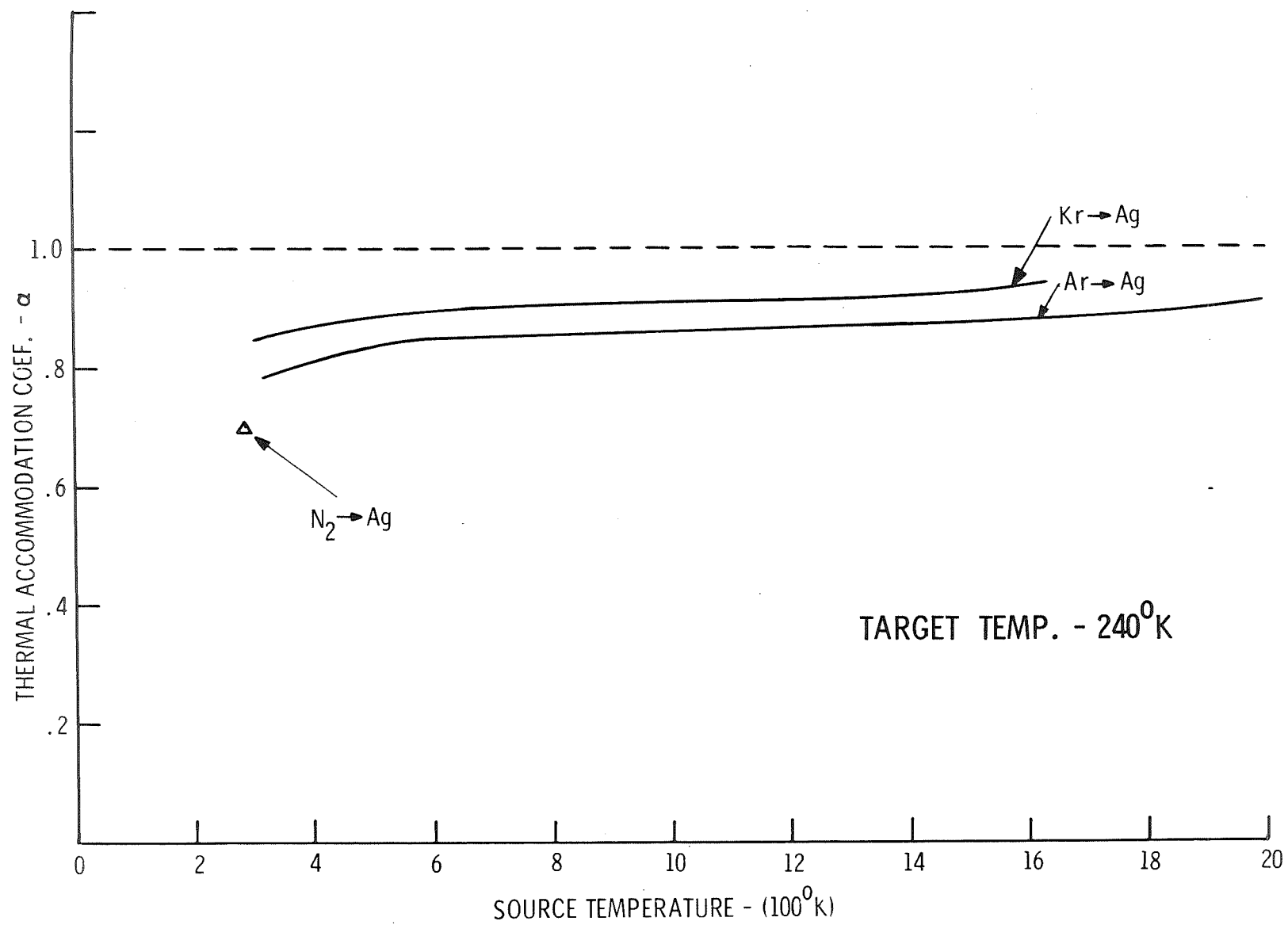
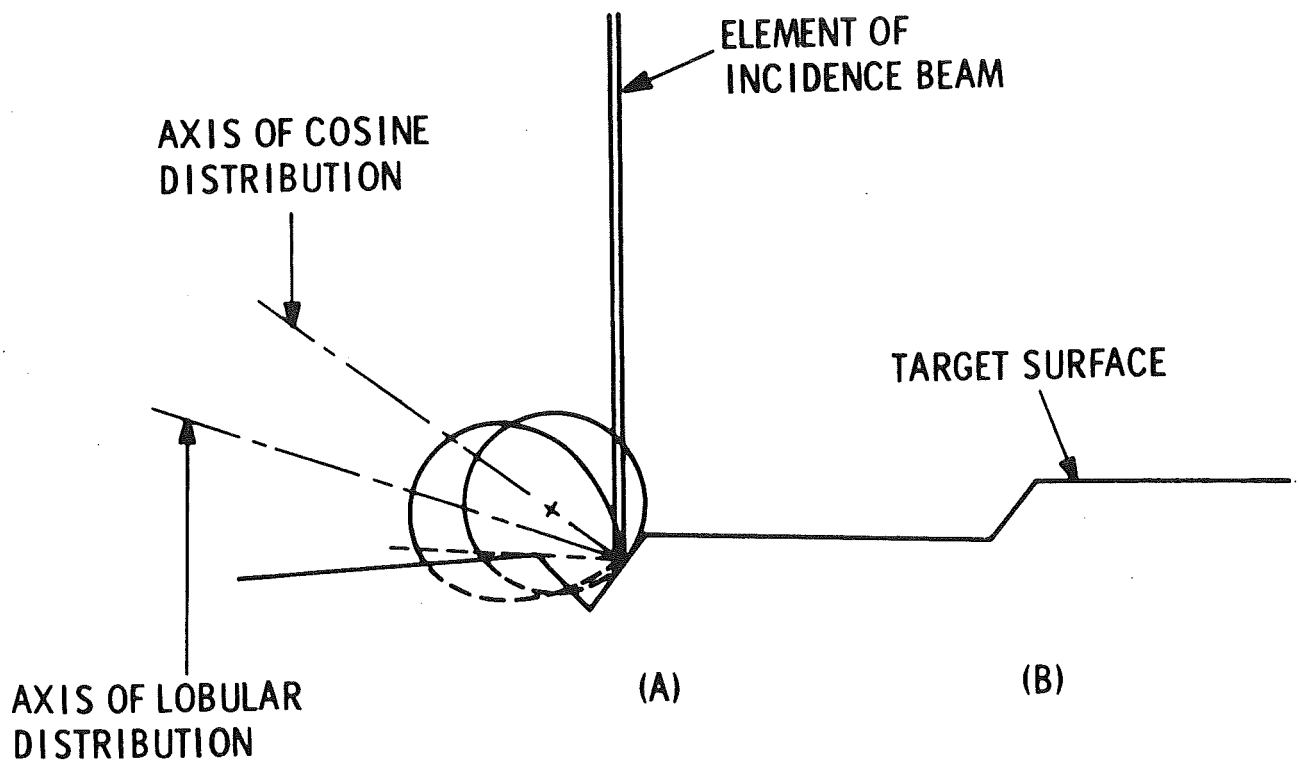


Figure 35



N 103-820

Figure 36

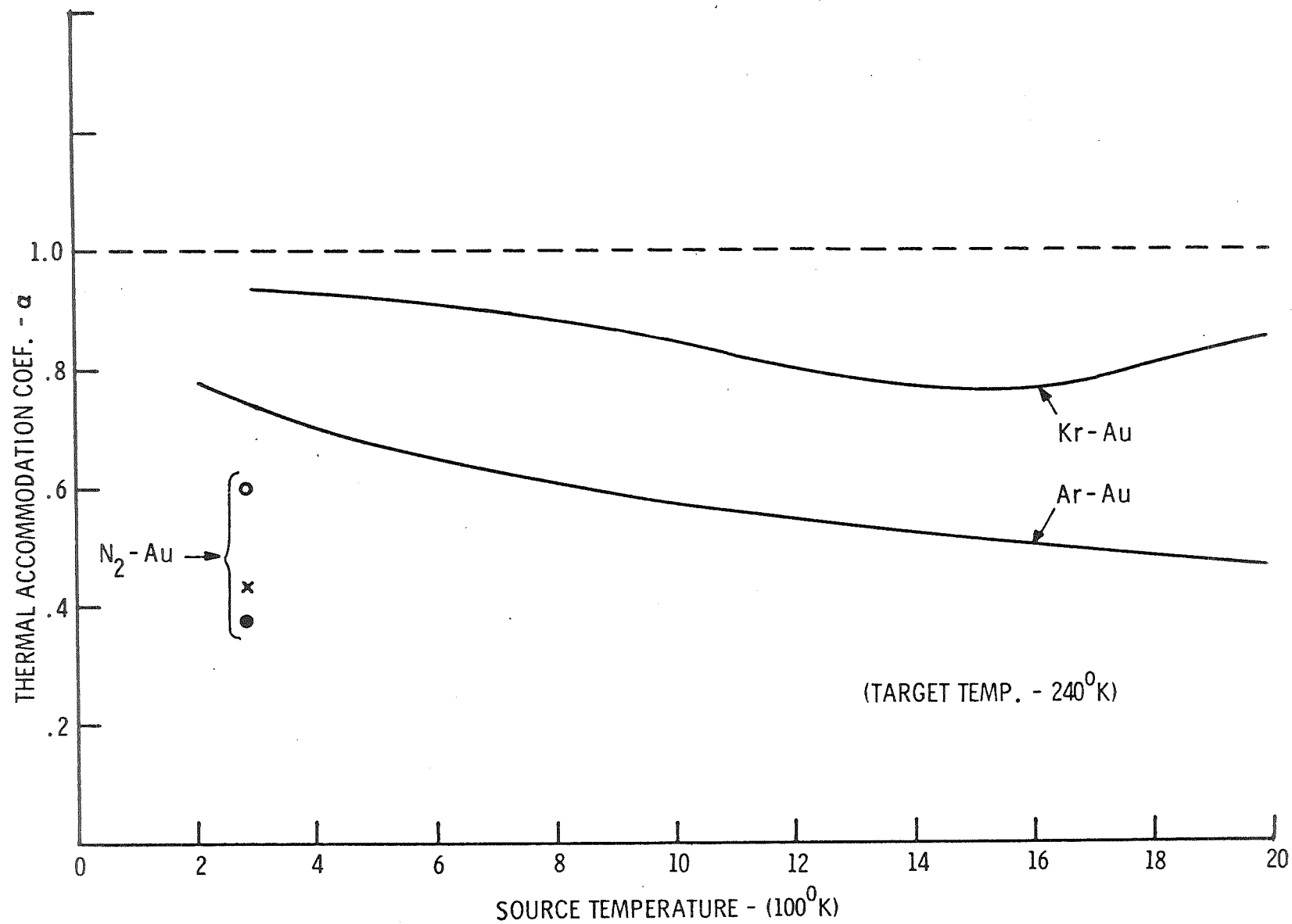


Figure 37

TABLE I

| Interaction                     | $T_i$<br>(°K) | $T_c^*$<br>(°K) | Angle of $\dagger$<br>Incidence | $R_\theta$ | Comments            |
|---------------------------------|---------------|-----------------|---------------------------------|------------|---------------------|
| Ar $\rightarrow$ mica           | 279           | 240             | 0°                              | 0.98       |                     |
| Ar $\rightarrow$ mica           | 279           | 240             | 0°                              | 0.96       |                     |
| Ar $\rightarrow$ mica           | 279           | 240             | 72°                             | 0.71       |                     |
| Ar $\rightarrow$ Au             | 279           | 240             | 0°                              | 1.00       | First Gold Deposit  |
| Ar $\rightarrow$ Au             | 279           | 240             | 72°                             | 0.68       |                     |
| Au $\rightarrow$ Au             | 892           | 240             | 0°                              | 1.05       |                     |
|                                 |               | 240             | 72°                             | 0.684      |                     |
| Ar $\rightarrow$ Au             | 1458          | 240             | 0°                              | 1.22       |                     |
|                                 |               | 240             | 72°                             | 0.75       |                     |
| N <sub>2</sub> $\rightarrow$ Au | 279           | 240             | 0°                              | 1.05       |                     |
|                                 |               |                 | 36°                             | 0.92       |                     |
|                                 |               |                 | 72°                             | 0.69       |                     |
| Ar $\rightarrow$ Au             | 279           |                 | 0°                              | 1.00       | Second Gold Deposit |
|                                 |               |                 | 72°                             | 0.68       |                     |
| Ar $\rightarrow$ Au             | 1536          |                 | 0°                              | 1.20       |                     |
|                                 |               |                 | 72°                             | 0.70       |                     |
| Ar $\rightarrow$ Au             | 288           |                 | 0°                              | 0.99       | Third Gold Deposit  |
|                                 |               |                 | 72°                             | 0.69       |                     |
| Kr $\rightarrow$ Au             | 279           |                 | 0°                              | 0.99       |                     |
|                                 |               |                 | 72°                             | 0.72       |                     |
| Ar $\rightarrow$ Au             | 1761          |                 | 0°                              | 1.20       |                     |
|                                 |               |                 | 72°                             | 0.72       |                     |
| Ar $\rightarrow$ Au             | 1793          |                 | 0°                              | 1.20       |                     |
|                                 |               |                 | 72°                             | 0.70       |                     |

Notes

\* Since the thermocouple circuit was open an estimated value of  $T_c$  is used. This estimate is based on extrapolation of data obtained from previous runs. Fortunately the value of  $\alpha$  is relatively insensitive to the square root of the ratio of  $T_c$  to  $T_i$ .

$\dagger$  The angle of incidence is measured from the surface normal.

TABLE II

|   | Interaction        | Source<br>Temp ( $^{\circ}\text{K}$ ) | $R_o$ | $R_{75}$ |
|---|--------------------|---------------------------------------|-------|----------|
| A | Ar-Au              | 288                                   | 1.00  |          |
|   |                    | 993                                   | 1.027 |          |
|   |                    | 1733                                  | 1.05  |          |
|   |                    | 288                                   |       | .660     |
|   |                    | 1735                                  |       | .715     |
|   | N <sub>2</sub> -Au | 288                                   | 1.08  |          |
|   | Ar-Au              | 288                                   | 1.015 |          |
|   |                    | 1723                                  | 1.000 |          |
|   | N <sub>2</sub> -Au | 288                                   | 1.05  |          |
|   |                    |                                       |       |          |
| B | Ar-Au              | 288                                   | 1.047 |          |
|   |                    | 1728                                  | 1.21  |          |
|   |                    | 1740                                  |       | .673     |
|   |                    | 288                                   |       | .71      |
|   | N <sub>2</sub> -Au | 288                                   | 1.035 |          |
|   | N <sub>2</sub> -Au | 288                                   | 1.03  |          |
|   |                    |                                       |       |          |
| C | Ar-Al              | 288                                   | 1.076 |          |
|   |                    | 1745                                  | 1.25  |          |
|   |                    | 288                                   | 1.09  |          |
|   |                    | 1740                                  | 1.248 |          |
|   |                    | 288                                   |       | .553     |
|   |                    | 1735                                  |       | .516     |
|   | N <sub>2</sub> -Al | 288                                   | 1.08  |          |
|   |                    |                                       |       |          |
|   | Ar-Al              | 288                                   | 1.07  |          |
|   |                    | 1000                                  | 1.198 |          |
|   |                    | 1733                                  | 1.31  |          |
|   |                    | 288                                   | 1.06  |          |
|   |                    | 288                                   |       | .608     |
|   |                    | 1735                                  |       | .596     |
| D | N <sub>2</sub> -Al | 288                                   | 1.000 |          |
|   | O <sub>2</sub> -Al | 288                                   | 1.005 |          |
|   | Ar-Al              | 288                                   | 1.01  |          |
|   |                    | 1735                                  | 1.197 |          |
|   | N <sub>2</sub> -Al | 550                                   | 1.05  |          |
|   |                    | 550                                   |       | .710     |

NOTE: 1) Condition A - contaminated gold  
 B - clean gold  
 C - clean aluminum  
 D - aluminum exposed to oxygen

2) Target temperature  $243^{\circ}\text{K}$  throughout

The average values of the force ratio,  $R = F_o/F_c^*$ , are tabulated below:

TABLE III

| <u>Gas</u> | <u>Source<br/>Temp.<br/>(°K)</u> | <u>Target<br/>Temp.<br/>(°K)</u> | <u>Target Material</u> |              |             |             |                 |
|------------|----------------------------------|----------------------------------|------------------------|--------------|-------------|-------------|-----------------|
|            |                                  |                                  | <u>Al</u>              | <u>Brass</u> | <u>Mica</u> | <u>BeCu</u> | <u>Ag Paint</u> |
|            |                                  |                                  | $R_2$                  | $R_3$        | $R_4$       | $R_5$       | $R_6 = F_o/F_c$ |
| Argon      | 288                              | 164                              | 1.036                  | 1.028        | 1.02        | 1.03        | 1.025           |
|            | 1653                             | 164                              | 1.013                  | ---          | ---         | 1.028       | ---             |
| Nitrogen   | 288                              | 164                              | 1.012                  | 1.042        | 1.033       | 1.01        | 1.038           |
|            | 572                              | 164                              | 1.013                  | ---          | ---         | 1.128       | ---             |

\*  $F_o$  is the force on the test surface and  $F_c$  is the force on the cavity.

## SECTION 5

### CONCLUSIONS

The results of this investigation show that, in general, particles scattered from either clean or contaminated noncrystalline surfaces do not have a cosine spatial distribution. At grazing angles of incidence, the tendency to a lobular pattern increases both with incident energy and increasing angle of incidence. This behavior is consistent with momentum transfer or drag measurements on the test surfaces. Even at normal incidence, the flux distribution is found to be noncosine.

The flattening which was observed may account for the fact the values of  $R_o$  less than unity were occasionally measured. In all cases, the lobular distributions became less pronounced, i.e., more cosine like, with surface aging.



SECTION 6  
REFERENCES

1. Goodman, F. O., and Wachman, H. Y., Formula for Thermal Accommodation Coefficient, Figures 2, 3, 4, 5 and References 6, 7, 17, 18.
2. Shamberg, R., Analytic Representation of Surface Interaction for Free Molecular Flow with Application to Drag of Various Bodies, Rand Corp. Report R-339, Section 12, Santa Monica, Calif., June 1959.
3. General Electric Spacecraft Department, private communication (1966).
4. Trilling, R., "Thermal Accommodation of Rare Gases on Clean Metal Surfaces," Proceedings of Rarefied Gas Dynamics Symposium, 1966 Academic Press.
5. Goodman, F. O., J. Phys.Chem. Solids, Vol. 24, p. 1451, (1963)
6. Goodman, F. O., J. Phys. Chem. Solids, Vol. 26, p. 35, (1965).